J. Fluid Mech. (2019), *vol.* 875, *pp.* 173–224.
doi:10.1017/jfm.2019.481

Study of wave effect on vorticity in Langmuir turbulence using wave-phase-resolved large-eddy simulation

Anqing Xuan[1], Bing-Qing Deng[1] and Lian Shen[1,†]

[1]Department of Mechanical Engineering and Saint Anthony Falls Laboratory, University of Minnesota, Minneapolis, MN 55455, USA

(Received 30 December 2018; revised 10 June 2019; accepted 11 June 2019; first published online 18 July 2019)

The effects of a water surface wave on the vorticity in the turbulence underneath are studied for Langmuir turbulence using wave-phase-resolved large-eddy simulation. The simulations are performed on a dynamically evolving wave-surface-fitted grid such that the phase-resolved wave motions and their effects on the turbulence are explicitly captured. This study focuses on the vorticity structures and dynamics in Langmuir turbulence driven by a steady and co-aligned progressive wave and surface shear stress. For the first time, the detailed vorticity dynamics of the wave–turbulence interaction in Langmuir turbulence in a wave-phase-resolved frame is revealed. The wave-phase-resolved simulation provides detailed descriptions of many characteristic features of Langmuir turbulence, such as elongated quasi-streamwise vortices. The simulation also reveals the variation of the strength and the inclination angles of the vortices with the wave phase. The variation is found to be caused by the periodic stretching and tilting of the wave orbital straining motions. The cumulative effect of the wave on the wave-phase-averaged vorticity is analysed using the Lagrangian average. It is discovered that, in addition to the tilting effect induced by the Lagrangian mean shear gradient of the wave, the phase correlation between the vorticity fluctuations and the wave orbital straining is also important to the cumulative vorticity evolution. Both the fluctuation correlation effect and the mean tilting effect are found to amplify the streamwise vorticity. On the other hand, for the vertical vorticity, the fluctuation correlation effect cancels the mean tilting effect, and the net change of the vertical vorticity by the wave straining is negligible. As a result, the wave straining enhances only the streamwise vorticity and cumulatively tilts vertical vortices towards the streamwise direction. The above processes are further quantified analytically. The role of the fluctuation correlation effect in the wave-phase-averaged vorticity dynamics provides a deeper understanding of the physical processes underlying the wave–turbulence interaction in Langmuir turbulence.

Key words: wave–turbulence interactions, ocean processes

† Email address for correspondence: shen@umn.edu

1. Introduction

Turbulence in the upper ocean is crucial to the transport of momentum, mass and heat (Leibovich 1983; McWilliams & Sullivan 2000; Kukulka *et al.* 2009; D'Asaro 2014). Notably, Langmuir turbulence, often present when wind blows over surface waves, is considered one of the most common types of upper-ocean turbulence. Langmuir turbulence is important to many geophysical applications, including air–sea interactions (Thorpe 2004; Sullivan & McWilliams 2010), global climate (Fan & Griffies 2014; Li *et al.* 2016), transport of bubbles and pollutants (Li 2000; Thorpe *et al.* 2003; Yang, Chamecki & Meneveau 2014*a*; Yang *et al.* 2015) and marine ecosystems (Lewis 2005).

Langmuir turbulence is characterised by the presence of an array of long and counter-rotating vortical structures under the water surface. First studied by Langmuir (1938), these underwater motions are referred to as Langmuir circulations. The circulating structures induce the amalgamation of buoyant materials, such as algae and foam, on the surface, forming long and narrow bands called windrows.

There have been several theories on the generation of Langmuir circulations. The most notable one is the Craik–Leibovich (CL) theory (Craik & Leibovich 1976; Leibovich 1977*b*), which utilizes a wave–current interaction mechanism to explain the causes of Langmuir circulations. Because the wave period is usually much shorter than the characteristic time scales of the current and Langmuir circulations, the current motions are averaged over multiple wave periods and the equations (CL equations) describing the averaged current motions are obtained. The time-averaged wave effect on the long-term evolution of the current motions is modelled as a vortex force, $\boldsymbol{u}_s \times \boldsymbol{\omega}$, an outer product of the averaged vorticity $\boldsymbol{\omega}$ and the Stokes drift of the wave $\boldsymbol{u}_s$. The CL equations are easy to use because the waves do not need to be explicitly resolved.

In recent years, numerical simulations based on the CL equations, especially those using large-eddy simulation (LES) (see e.g. Skyllingstad & Denbo 1995; McWilliams, Sullivan & Moeng 1997; Li, Garrett & Skyllingstad 2005; Tejada-Martínez & Grosch 2007; Harcourt & D'Asaro 2008; Grant & Belcher 2009; Kukulka *et al.* 2009; Sullivan *et al.* 2012; Deng *et al.* 2019), have been successful in reproducing many features of the Langmuir circulations observed in the field and have advanced our understanding of the Langmuir circulations in the turbulence setting. Langmuir circulations are now considered as the turbulent coherent structures arising from the wave–turbulence interaction, and span a wide range of spatial and temporal scales (Thorpe 2004).

The wave–turbulence interaction problem is complex, partially because the Lagrangian and Eulerian aspects of the surface gravity wave introduce different time scales on which the wave interacts with the subsurface turbulence. The Stokes drift in the vortex force describes the Lagrangian transport of fluid particles by the wave (Stokes 1847; Longuet-Higgins 1953). The Stokes drift velocity is used in the CL equations to model the accumulative long-term distortion effects of the wave on the turbulence. Other than the accumulative drift, a progressive wave has an orbital velocity field that induces a straining field that varies periodically with the wave phase. As a result, the turbulence underneath the surface wave undergoes alternating stretching and shear straining within a wave period as the wave passes by. Since the CL equations describe only the long-term averaged flow, the motions with a time scale shorter than a wave period are not resolved.

The direct modulation effects of the wave on the turbulence have been studied by several theoretical (Teixeira & Belcher 2002), experimental (Jiang & Street 1991;

Rashidi, Hetsroni & Banerjee 1992) and numerical (Guo & Shen 2013, 2014) works. Turbulence statistics, such as the Reynolds stress, are found to vary with the wave phase. The coherence between the turbulence and wave phase is also observed in field measurements (Veron, Melville & Lenain 2009). However, existing theoretical and numerical studies are often restricted to the simple isotropic turbulence set-up and shear-free surface condition, which lacks the surface wind shear and therefore has different turbulence forcing from the Langmuir turbulence. Experimental measurements, on the other hand, are often challenging in the near-surface region to obtain precise quantifications of turbulence modulation by the wave. The works cited above, however, have suggested the important role of wave-phase-correlated turbulence fluctuations in the wave–turbulence interactions and the necessity to further study the modelling of the wave effects.

Furthermore, the vortex force modelling of the cumulative wave effect in the CL equations has not been directly validated, especially under a turbulence setting, therefore the validity of the modelling still remains indefinite. There have been a few numerical simulations of Langmuir circulations with phase-resolved wave (Zhou 1999; Kawamura 2000; Fujiwara, Yoshikawa & Matsumura 2018; Wang & Özgökmen 2018), which have provided some comparisons with the CL theory. The above works found that, although the flow statistics from the wave-phase-resolved simulations and CL simulations are qualitatively similar, some results are different quantitatively. Zhou (1999) and Wang & Özgökmen (2018) found that the CL simulations produce weaker Langmuir circulations than the wave-phase-resolved simulations due to the lack of the Eulerian mean drift associated with a viscous gravity wave. However, the conclusion is drawn from simulations using a constant eddy viscosity. Zhou (1999) also performed LES of Langmuir turbulence under an explicit surface wave and found that the wave-phase-resolved simulation results in stronger turbulence than the CL-based LES, which is attributed to the lack of the fast turbulence fluctuations that have time scales similar to the waves in the CL-based LES. This again implies that the wave-phase-correlated turbulence fluctuations that are filtered out in the CL equations can be important to the dynamics of Langmuir turbulence.

The present study aims to use wave-phase-resolved LES to perform a detailed study of the vorticity dynamics to shed light on the mechanisms of the generation and evolution of the Langmuir circulations, specifically the effects of wave straining and wave-phase-correlated turbulence fluctuations. Focusing on the fundamental mechanisms of wave–turbulence interaction, we consider a canonical set-up, where a turbulent flow is driven by a monochromatic progressive wave and a prescribed shear stress on the surface that are aligned in the same direction, corresponding to the classical modelling of the CL theory (e.g. Craik 1977; Leibovich 1977*a*). The simulations are carried out in a dynamically moving, wave-surface-fitted domain (Yang & Shen 2011; Xuan & Shen 2019). The simulations resolve the wave and turbulent motions directly, such that both the instantaneous and cumulative effects of the wave on the turbulence are captured.

Our simulations reveal detailed information about the wave-phase variation of the vorticity statistics and the effects of wave straining on the variation of vorticity. The cumulative effect of wave straining on vorticity is further analysed through the Lagrangian average of the terms in the vorticity evolution equations to obtain an understanding of the wave-phase-averaged vorticity evolution. It is found that the correlations between the wave-phase variation of the vorticity and the wave orbital straining are important to the long-term evolution of the vorticity. The correlation effect contributes to the growth of the streamwise vorticity, but offsets the change

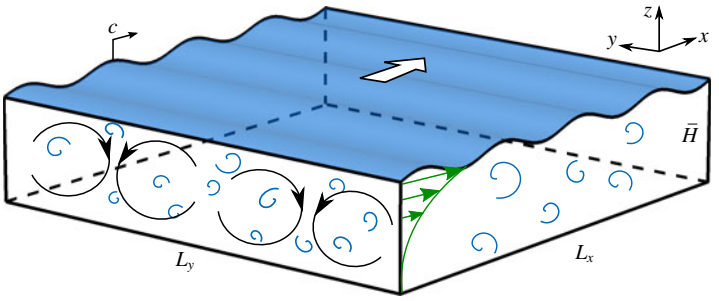

FIGURE 1. (Colour online) Sketch of the simulation set-up. The hollow arrow on the surface indicates the direction of wave propagation (with phase speed c) and surface shear stress.

of vertical vorticity, resulting in an increase in the streamwise vorticity only. The mechanism of the correlation effect is then explained in this study with detailed analytical quantification, providing a deeper understanding of the vorticity dynamics in wave–turbulence interactions.

This paper is organized as follows. In § 2, the problem set-up, numerical method and simulation parameters are given. A triple decomposition method that separates the current, wave and turbulence is also introduced in § 2 as the basis of the subsequent analyses. In § 3, the flow features of the Langmuir turbulence captured by our wave-phase-resolved simulations, including an overview of the wave-phase-modulation effect on the vortices, are presented. In § 4, the wave velocity field and the associated straining field are assessed, which facilitates the discussion of the vorticity distortion by the wave. Then, in § 5, we perform detailed analyses of the variation of the turbulence vorticity with the wave phase and its mechanism. In § 6, the Lagrangian vorticity evolution is analysed, with focus on the cumulative effect of the wave straining on the vorticity. The conclusions of this paper and suggestions for future studies are given in § 7.

2. Problem set-up and numerical methods

In this section, we first introduce the problem set-up and governing equations in §§ 2.1 and 2.2. Then, the numerical method and the computational parameters are described in §§ 2.3 and 2.4, respectively. Finally, in § 2.5, we introduce a triple decomposition method that employs the theory of generalized Lagrangian mean (GLM) (Andrews & Mcintyre 1978) to decompose the flow motions into the current, wave and turbulence for the subsequent analyses.

2.1. *Problem set-up*

For the mechanistic study of the wave–turbulence interaction processes, we consider a statistically steady turbulent flow driven by a monochromatic progressive wave, with a constant surface shear stress representing the wind shear applied on the surface. The simulations are performed in a horizontally periodic box bounded by a surface wave, as shown in figure 1. The wave propagation direction and the surface stress direction are aligned in the x-direction. The shear stress is tangential to the wave surface in the x–z plane. A dynamic pressure forcing is imposed on the surface to keep the waves from decaying or distortion (Guo & Shen 2009). With the constant wave

and shear stress forcing, the Langmuir turbulence develops and reaches a statistically steady state, based on which we perform the analyses on the vorticity dynamics. We also note that the present study of Langmuir turbulence is different from the previous study of isotropic turbulence below a surface wave by Guo & Shen (2013, 2014). In Langmuir turbulence, the turbulence is generated due to the wind shear applied at the wave surface and is modulated by the wave (Craik 1977; Leibovich 1977*a*; Leibovich & Paolucci 1980, 1981). By contrast, in Guo & Shen (2013, 2014), no wind shear stress is applied at the surface and isotropic turbulence is generated by a random force in the bulk flow. Therefore, these are two different problems.

Because the present study focuses on the fundamental mechanism of the wave effect on the turbulence, we intentionally maintain a stationary surface wave to isolate the dynamical processes in the turbulence. We shall note that the current and turbulence underneath can also affect the wave field, including changing the dispersion relation (Kirby & Chen 1989; Swan, Cummins & James 2001) and inducing wave scattering and damping (Vivanco & Melo 2004; Ardhuin & Jenkins 2006; Gutiérrez & Aumaître 2016). Although the wave-phase-resolved simulation can be used to study the turbulence effect on the surface waves and the effect of temporal variation of the wave on the turbulence (Phillips 2002), they are beyond the scope of this research. In addition, as discussed in the following sections, the current and turbulence resulting from the set-up are weak compared with the wave orbital motions, and the wave field evolves slowly compared with the wave period (Thorpe 2004). Therefore, it is reasonable to maintain a steady wave such that the wave effect on the turbulence can be quantified accurately.

2.2. *Governing equations and boundary conditions*

In this study, the turbulent flow is modelled by LES. For a fluid with constant density ρ and kinematic viscosity ν, the grid-resolved flow motions in an Earth-fixed Eulerian frame are described by the filtered incompressible Navier–Stokes equations and continuity equation,

$$\frac{\partial u_i}{\partial t} + \frac{\partial (u_i u_j)}{\partial x_j} = -\frac{1}{\rho}\frac{\partial p}{\partial x_i} + \nu \frac{\partial^2 u_i}{\partial x_j x_j} - \frac{\partial \tau_{ij}^d}{\partial x_j}, \tag{2.1}$$

$$\frac{\partial u_j}{\partial x_j} = 0. \tag{2.2}$$

In the above equations, x_i $(i = 1, 2, 3)$ denote the Cartesian coordinates (x, y, z), respectively; u_i denote the components of the filtered Eulerian velocity (u, v, w); $\tau_{ij}^d = \tau_{ij} - \tau_{ii}/3$ $(i, j = 1, 2, 3)$ is the trace-free part of the subgrid-scale (SGS) stress τ_{ij}; and p is the modified dynamic pressure, which includes the isotropic part of the SGS stress $\tau_{ii}/3$.

At the free surface $z = \eta(x, y)$, where η is the surface elevation, we impose a constant tangential shear stress τ_0 in the x–z plane and a dynamic pressure p_a. The value of p_a is determined based on the wave surface elevation and the surface velocity to maintain a monochromatic progressive wave (Guo & Shen 2009). The work done by p_a compensates the wave energy loss such that the wave amplitude is sustained. The detailed form of p_a is given in appendix A. The stress balance at the interface is given by the dynamic boundary conditions (DBCs),

$$\boldsymbol{n} \cdot \boldsymbol{\sigma} \cdot \boldsymbol{n}^{\mathrm{T}} = -p_a, \tag{2.3a}$$

$$\boldsymbol{t}^1 \cdot \boldsymbol{\sigma} \cdot \boldsymbol{n}^{\mathrm{T}} = \tau_0, \tag{2.3b}$$

$$\boldsymbol{t}^2 \cdot \boldsymbol{\sigma} \cdot \boldsymbol{n}^{\mathrm{T}} = 0. \tag{2.3c}$$

The above equations relate the pressure p_a and shear stress τ_0 to the total stress tensor $\boldsymbol{\sigma} = -(p - \rho g z)\boldsymbol{I} + 2\rho\nu\boldsymbol{S}$, where $\boldsymbol{I}$ is the identity tensor, g is the gravitational acceleration and $\boldsymbol{S} = (\boldsymbol{\nabla u} + \boldsymbol{\nabla u}^{\mathrm{T}})/2$ is the resolved strain rate tensor. Also in the above equations, $\boldsymbol{n}$ is the surface normal vector; $\boldsymbol{t}^1$ and $\boldsymbol{t}^2$ are the surface tangential vectors in the x–z and y–z planes, respectively. These vectors are calculated by

$$\boldsymbol{n} = \frac{(-\eta_x, -\eta_y, 1)}{\sqrt{\eta_x^2 + \eta_y^2 + 1}}, \quad \boldsymbol{t}^1 = \frac{(1, 0, \eta_x)}{\sqrt{1 + \eta_x^2}}, \quad \boldsymbol{t}^2 = \frac{(0, 1, \eta_y)}{\sqrt{1 + \eta_y^2}}, \tag{2.4a–c}$$

where η_x and η_y denote $\partial\eta/\partial x$ and $\partial\eta/\partial y$, respectively.

The evolution of η is governed by the kinematic boundary condition (KBC),

$$\frac{\partial \eta}{\partial t} = w - u\eta_x - v\eta_y, \quad \text{at } z = \eta. \tag{2.5}$$

We note here that the SGS effect on the free-surface boundary conditions is still an open problem but is usually considered to be negligibly small (Hodges & Street 1999; Dimas & Fialkowski 2000). Meanwhile, the SGS effect on the boundary is minimized in the present study with a sufficient grid resolution to achieve wall-resolved LES (§ 2.4).

The bottom is free slip, where the velocity boundary condition is given by

$$\frac{\partial u}{\partial z} = \frac{\partial v}{\partial z} = 0, \quad w = 0, \quad \text{at } z = -\bar{H}. \tag{2.6}$$

Because the shear is often weak at the base of the ocean surface boundary layer (Belcher *et al.* 2012), the free-slip boundary condition is imposed to minimize the impact of the bottom of the domain as long as $\bar{H}$ is sufficiently large (Shen *et al.* 1999). Under realistic conditions, body forces such as the Coriolis force balance the momentum. In this study, to focus on the mechanisms of the wave–turbulence interaction, we use a uniform adverse pressure gradient $\partial p/\partial x = \tau_0/\bar{H}$ to balance the shear stress at the upper surface so that the total momentum in the flow does not increase with time, which facilitates the analyses of statistics. The imposed pressure gradient is small compared to other effects (especially the wave forcing) in the system, therefore ought not to qualitatively change the fundamental mechanisms of the wave–turbulence interaction that we are interested in. More details of the magnitude of the forcing are discussed in § 2.4.

The SGS stress τ_{ij}^d in (2.1) is computed using a Lagrangian dynamic scale-dependent model (Bou-Zeid, Meneveau & Parlange 2005)

$$\tau_{ij}^d = -2C_\Delta |S_{ij}| S_{ij}, \tag{2.7}$$

where $|S_{ij}| = \sqrt{2S_{ij}S_{ij}}$ is the magnitude of the tensor S_{ij} and C_Δ is the Smagorinsky coefficient. The C_Δ is dynamically determined based on the weighted average of the flow information along pathlines. The dynamic model removes the necessity to determine C_Δ on an *ad hoc* basis (Germano *et al.* 1991), and the Lagrangian average formulation improves the model's capability to address the inhomogeneity in flows with complex geometries (Meneveau, Lund & Cabot 1996; Stoll & Porté-Agel 2006; Yang, Meneveau & Shen 2014*b*,*c*), such as the waves in the present study. This model also takes the scale dependency of C_Δ into consideration. Traditional dynamic

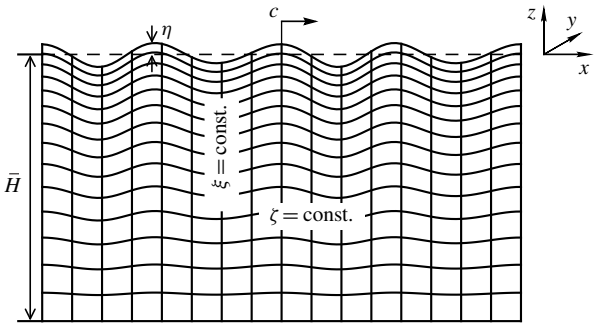

FIGURE 2. Curvilinear coordinates used in the simulations. Only one x–z (ξ–ζ) plane is shown.

model applies a test filter with scale $\widetilde{\Delta}$ (typically $\widetilde{\Delta} = 2\Delta$) to the resolved velocity and calculates C_Δ using the flow information at both grid filter scale and test filter scale. The calculation utilizes the assumption that C_Δ does not depend on the filter scale, i.e. $C_\Delta = C_{\widetilde{\Delta}}$. However, it is found that the scale-invariance assumption does not always hold, especially near the boundary (Porté-Agel, Meneveau & Parlange 2000). The scale-dependent model introduces another test filter with width $\hat{\Delta}$ (e.g. $\hat{\Delta} = 2\widetilde{\Delta} = 4\Delta$) and is thus able to determine how the Smagorinsky coefficient varies with the filter width using three levels of the filtered flow fields. This tuning-free scale-dependent model has been shown to yield good predictions of near-surface flow features (Porté-Agel *et al.* 2000).

2.3. *Numerical methods*

The governing equations (2.1) and (2.2) are transformed to and solved on a surface-boundary-fitted curvilinear coordinate system (ξ^i, τ). The numerical approach (Yang & Shen 2011; Xuan & Shen 2019) has been proven to be accurate and effective in resolving the flow details in the wave boundary layer, e.g. the distortion effects of waves on turbulence (Guo & Shen 2013, 2014) and wind–wave interactions (Yang, Meneveau & Shen 2013; Yang *et al.* 2014*c*).

The transformation between the Cartesian and curvilinear coordinates is defined as

$$\xi^1 = x_1, \quad \xi^2 = x_2, \quad \xi^3 = \frac{z + \bar{H}}{\eta + \bar{H}}, \quad \tau = t. \tag{2.8a–c}$$

Hereafter, (ξ^1, ξ^2, ξ^3) are also denoted as (ξ, ψ, ζ). In the transformation (2.8), the varying depth in the physical space is normalized to a unit dimension in the curvilinear coordinates ($0 \leqslant \zeta \leqslant 1$). As an example, the transformation of a vertical x–z plane is illustrated in figure 2, where the curvilinear coordinate curves for ξ and ζ are plotted schematically.

Applying (2.8) to (2.1) and (2.2), we obtain the governing equations under the curvilinear coordinates as

$$\begin{aligned}&\frac{\partial (J^{-1}u_i)}{\partial \tau} - \frac{\partial (J^{-1}U_g^j u_i)}{\partial \xi^j} + \frac{\partial (J^{-1}U_j u_i)}{\partial \xi^j} \\ &\quad = -\frac{\partial}{\partial \xi^j}\left(J^{-1}\frac{\partial \xi^j}{\partial x_i}p\right) + \frac{1}{Re}\frac{\partial}{\partial \xi^j}\left(J^{-1}g^{ij}\frac{\partial u_i}{\partial \xi^j}\right) - \frac{\partial}{\partial \xi^k}\left(J^{-1}\frac{\partial \xi^k}{\partial x_j}\tau_{ij}^d\right),\end{aligned} \tag{2.9}$$

$$\frac{\partial U^j}{\partial \xi^j} = 0. \tag{2.10}$$

Here, $U^i = u_k(\partial \xi^i/\partial x_k)$ is the contravariant velocity; $U_g^i = \delta_{k3}\eta_t \xi^3(\partial \xi^i/\partial x_k)$ is the contravariant grid velocity; $J = \det(\partial \xi^i/\partial x_j)$ is the Jacobian determinant of the transformation; $g^{ij} = (\partial \xi^i/\partial x_k)(\partial \xi^j/\partial x_k)$ is the metric tensor of the transformation. We remark that the above equations are written and discretized in a strong conservative form under the curvilinear coordinates. We find that this practice greatly improves the conservation of mass and momentum in the simulations. The velocity and time scales in Langmuir turbulence span over a wide range. The turbulent motions generally have much smaller velocity than the wave-induced orbital velocity, and have a much longer characteristic time scale of evolution than the wave period. The disparate scales make the simulation of turbulence prone to the contamination by numerical errors. We find that the strong conservative scheme greatly reduces the numerical errors in mass and momentum conservations (Xuan & Shen 2019).

The horizontal directions ξ and ψ are discretized by uniformly distributed Fourier collocation points. The spatial derivatives with respect to ξ and ψ are obtained in the spectral space. The discretization in the ζ-direction employs a second-order finite-difference scheme, which allows more flexibility in the grid distribution to have fine resolution near the water surface. A staggered arrangement of the locations of the dependent variables is used in the ζ-direction to avoid the odd–even decoupling. The velocity components (u, v), (U, V) and the pressure p are located at the cell centre, while w and W are located half a grid spacing off at the cell face.

The solution of the Navier–Stokes equations (2.10) is coupled with the evolution of the free surface. The surface elevation $\eta(x, y, t)$ is obtained from the integration of (2.5) using a two-stage Runge–Kutta scheme,

$$\text{Stage I:} \quad \hat{\eta} = \eta|_t + \Delta t(w - u\eta_x - v\eta_y)|_t, \tag{2.11a}$$

$$\text{Stage II:} \quad \eta|_{t+\Delta t} = \hat{\eta} - \frac{\Delta t}{2}(w - u\eta_x - v\eta_y)|_t + \frac{\Delta t}{2}(\hat{w} - \hat{u}\hat{\eta}_x - \hat{v}\hat{\eta}_y), \tag{2.11b}$$

where $\hat{(\cdot)}$ denotes the intermediate prediction at $t + \Delta t$, and $(\cdot)|_t$ denotes the terms evaluated at time t. In each stage after obtaining η, the Navier–Stokes equations (2.9) are integrated using a fractional-step method (Kim & Moin 1985) to update the velocity in the new domain bounded by the water surface. The procedures to advance the system from t to $t + \Delta t$ are as follows,

(i) Obtain $\hat{\eta}$ using (2.11*a*).
(ii) Calculate $\hat{\boldsymbol{u}}$ and $\hat{p}$ in the domain with the elevation $\hat{\eta}$ by integrating equations (2.9) from t to $t + \Delta t$ subject to the constraint (2.10).
(iii) Obtain the corrected surface elevation $\eta|_{t+\Delta t}$ using (2.11*b*).
(iv) Calculate $\boldsymbol{u}$ and p in the domain with the elevation $\eta|_{t+\Delta t}$ by integrating (2.9) again from t to $t + \Delta t$ as in the step (ii), but with the corrected elevation $\eta|_{t+\Delta t}$.

The velocity and pressure obtained from the above step (iv) are the solution of the flow field at $t + \Delta t$. The above method has been tested extensively by Xuan & Shen (2019).

2.4. *Computational parameters*

In the present study, we mainly focus on the effects of the wave on the turbulence, therefore simulations with different turbulent Langmuir numbers $La_t = \sqrt{u_*/U_s}$

Case	La_t	ak	c/u_*	$\omega/u_*\bar{H}^{-1}$	Fr	$ak\omega/u_*\bar{H}^{-1}$
L1	0.35	0.084	1.16×10^3	4.05×10^3	4.62×10^{-4}	3.40×10^2
L1S	0.35	0.15	3.63×10^2	1.27×10^3	1.47×10^{-3}	1.90×10^2
L2	0.5	0.084	5.67×10^2	1.93×10^3	9.43×10^{-4}	1.67×10^2
L3	0.9	0.084	1.75×10^2	6.12×10^2	3.05×10^{-3}	51.44
S	∞	—	—	—	—	—

TABLE 1. Computational parameters of Langmuir turbulence in the present study.

and wave steepness ak are considered (table 1). The turbulent Langmuir number (McWilliams *et al.* 1997) associated with the friction velocity of wind-driven shear u_* and the surface Stokes drift U_s is an important dimensionless parameter quantifying the relative strength of wind shear forcing versus wave forcing. A smaller La_t indicates stronger wave effects and stronger Langmuir turbulence. The friction velocity u_* is associated with the imposed shear stress τ_0 by $u_* = \sqrt{\tau_0/\rho}$. The La_t ranges from 0.35 to 0.9, corresponding to cases with strong to weak wave forcing. Strong Langmuir turbulence is expected when the wave forcing dominates over the shear stress forcing. The flow features change to those of the shear-driven turbulence as La_t increases (Li *et al.* 2005). The La_t values considered above are consistent with the range of typical ocean conditions (Thorpe 2004). The case S is a pure shear-driven turbulent flow with no prescribed waves for comparison with the Langmuir turbulence cases. For cases L1, L2 and L3, we set the wave steepness ak to 0.084, where a and k are the amplitude and the wavenumber of the surface wave, respectively. A case L1S with a steeper wave but the same La_t as in case L1 is set up to study the effects of wave steepness. The dimensionless wavenumber $k\bar{H}$ is set to 3.5, corresponding to a deep-water wave with wavelength $\lambda = 4\pi\bar{H}/7$. The remaining wave-related parameters in table 1 are derived from La_t, ak and $k\bar{H}$ using the estimation from the linear wave theory. The surface Stokes drift is related to the wave phase speed c through $U_s = (ak)^2 c$ according to the linear wave theory, and thus $c/u_* = (ak)^{-2} La_t^{-2}$. The wave frequency $\omega = ck$ normalized by the shear strain rate $u_*/\bar{H}$ is $\omega/(u_*\bar{H}^{-1}) = (c/u_*)(k\bar{H})$, which also represents the ratio of the wave frequency to the frequency of the eddy turnover motion in the turbulent flow. Also given in table 1 is the Froude number $Fr = u_*/(g\bar{H})^{1/2} = u_*/c(k\bar{H})^{1/2}$. For reference, we provide an example of the typical dimensional parameters that correspond to case L1. The wavelength and the wavenumber for the surface wave are $\lambda = 60$ m and $k = 2\pi/\lambda = 0.105$ m^{-1}, respectively, which have been used in LES of Langmuir circulation (McWilliams *et al.* 1997; Li *et al.* 2005). The corresponding surface Stokes drift is $U_s = 0.068$ m s^{-1}, and the friction velocity is $u_* = 8.3 \times 10^{-3}$ m s^{-1}.

With the parameters above, we can compare the relative magnitudes of the different quantities in the system. As shown in table 1, the velocity scale of the current and turbulent motions, being $O(u_*)$, is much smaller than the wave phase speed c. As a result, it is expected that the modification of the current on the wave propagation is small. The separation of the velocity scales also corresponds to disparate forcing scales. The straining rate due to the wave orbital velocity, associated with the direct forcing of the wave applied on the turbulence, is $O(ak\omega)$. This is significantly larger than the shearing of the current, which is $O(u_*/\bar{H})$, as shown in the last column of table 1. Using the wave strain rate, the forcing of the wave straining on the turbulence is estimated to be $O(\rho ak\omega u_*)$, which is much larger than the applied pressure gradient $\rho u_*^2/\bar{H}$, also shown in the last column of table 1.

For the 60 m wave in oceans with a 8.3×10^{-3} m s^{-1} friction velocity discussed above, $Re_\tau = u_* \bar{H}/\nu$ is $O(10^5)$. To have the same Reynolds number, the LES would need wall-layer modelling. However, the accuracy of wall-layer modelling in wave-phase-resolved free-surface simulation is still unknown. Here, for the purposes of mechanistic study of wave–turbulence interactions and establishing an accurate dataset for future wall-layer modelling study, we choose to perform wall-resolved LES at a moderate Reynolds number $Re_\tau = 2000$ such that the near-surface dynamics of wave–turbulence interactions is captured accurately. We note that some previous CL equations based study of Langmuir turbulence also employed the wall-resolved LES approach with reduced Reynolds number to resolve the boundary layer for mechanistic study (see e.g. Tejada-Martínez *et al.* (2009) and more discussions in Deng *et al.* (2019) recently). In the future, after the wall-layer modelling is validated for wave-phase-resolved LES of free-surface turbulence, it would be desirable to perform wall-modelled wave-phase-resolved LES for Langmuir turbulence with realistic Reynolds number directly. All the simulations are performed in a domain with a size $L_x \times L_y \times \bar{H} = 16\pi\bar{H}/7 \times 16\pi\bar{H}/7 \times \bar{H}$. This domain allows four periods of the wave in the x-direction. The domain size is comparable with previous simulations based on the CL equations in terms of the ratio of the mixed layer depth to the horizontal lengths (McWilliams *et al.* 1997; Li *et al.* 2005; Kukulka *et al.* 2009). The domain size is further confirmed to be sufficiently large according to the two-point auto-correlation (appendix B). The domain is discretized by a grid of $288 \times 512 \times 217$ points. The horizontal discretization is uniform with the streamwise and spanwise grid resolutions being $\Delta x^+ = 49.9$ and $\Delta y^+ = 28.0$, respectively. The vertical grid is condensed near the free surface, where the minimum grid spacing is $\Delta z^+|_{min} = 0.49$. Here, the superscript '+' denotes the wall-unit length defined as $x_i^+ = x_i u_*/\nu$. The grid resolution satisfies the requirement of boundary-resolving approach, i.e. $\Delta x^+ \simeq 50$, $\Delta y^+ \simeq 30$ and $\Delta z^+|_{min} < 1$, which is needed for resolving the small-scale longitudinal vortical structures in the viscous sublayer that typically have a streamwise length of a few hundred wall units and a spanwise spacing of approximately 100 wall units (Chapman 1979; Piomelli & Balaras 2002; Choi & Moin 2012; Yang *et al.* 2013).

Simulations are initialized with a linear wave solution. Initial random disturbance is added to the near-surface region $kz > -0.2$ as seeds for turbulence generation. The shear stress is imposed on the wave surface when the simulation starts. The simulations run for at least 20 eddy turnover time $\bar{H}/u_*$, at which all cases reach the statistically steady state. Then, the simulations are run for another 25 eddy turnover time, which we find to be sufficiently long for statistical analyses.

2.5. *Triple decomposition and averaging techniques*

Because our wave-phase-resolved simulations capture the wave orbital motions, current and turbulent fluctuations simultaneously, it is important to decompose the flow motions so that we can consider the effects of different components separately. The total resolved velocity $\boldsymbol{u}$ is decomposed into the mean current $\boldsymbol{u}_c$, the wave orbital motions $\boldsymbol{u}_w$ and the turbulence fluctuation $\boldsymbol{u}'$, i.e.

$$\boldsymbol{u} = \boldsymbol{u}_c + \boldsymbol{u}_w + \boldsymbol{u}'. \tag{2.12}$$

Such decomposition is similar to the triple decomposition used for the analysis of the wind field over a progressive wave, where the velocity is decomposed into the mean velocity, wave-coherent velocity and turbulence (see e.g. Yang & Shen 2010;

Yang *et al.* 2014*b*). Each component of the total flow, including the current, wave motions and the turbulence, is obtained through a decomposition described below.

Assuming that both the mean current and the wave orbital motions are spanwise invariant and periodic with the wave period, the sum of the two can be obtained by a phase averaging as

$$\boldsymbol{u}_c + \boldsymbol{u}_w = \langle \boldsymbol{u} \rangle (x, z, t) = \frac{1}{4L_y T} \sum_{n=0}^{3} \left[\int_0^{L_y} \int_t^{t+T} \boldsymbol{u}(x + c\tau + n\lambda, y, z, \tau)\, \mathrm{d}\tau \mathrm{d}y \right]. \quad (2.13)$$

Here, T is the averaging period. The phase-averaging operator $\langle \cdot \rangle$ is essentially a spanwise averaging performed in the wave-following frame, and the average is also performed over the four waves (corresponding to $n = 0, 1, 2, 3$) in the domain due to the periodicity.

In $\langle \boldsymbol{u} \rangle$, the current part $\boldsymbol{u}_c$ and the wave part $\boldsymbol{u}_w$ are tangled together in a wavy domain. To separate them, we employ the GLM theory (Andrews & Mcintyre 1978), which provides an unambiguous way to separate the mean part (current) and the oscillatory part (wave motions) based on a Lagrangian description of the flow. We use the quasi-Eulerian mean velocity from the GLM theory as the current velocity $\boldsymbol{u}_c$, i.e.

$$\boldsymbol{u}_c = \overline{\boldsymbol{u}}^L - \boldsymbol{p}. \quad (2.14)$$

Then the wave component $\boldsymbol{u}_w$ is obtained as

$$\boldsymbol{u}_w = \langle \boldsymbol{u} \rangle - \boldsymbol{u}_c. \quad (2.15)$$

Here, $\overline{\boldsymbol{u}}^L$ is the Lagrangian mean velocity and $\boldsymbol{p}$ is the pseudo-momentum. Their definitions are given below.

The Lagrangian mean velocity $\overline{\boldsymbol{u}}^L$ is defined as

$$\overline{\boldsymbol{u}}^L(\boldsymbol{x}, t) = \frac{1}{T_L} \int_0^{T_L} \langle \boldsymbol{u} \rangle (\boldsymbol{x} + \delta \boldsymbol{x}(\boldsymbol{x}, \tau), \tau)\, \mathrm{d}\tau, \quad (2.16)$$

where T_L is the Lagrangian wave period (Longuet-Higgins 1986) and $\boldsymbol{x} + \delta \boldsymbol{x}$ is the trajectory of a fluid particle convected by the mean velocity $\langle \boldsymbol{u} \rangle$. The trajectory is expressed as a displacement $\delta \boldsymbol{x}(\boldsymbol{x}, t)$ relative to the mean position $\boldsymbol{x}$ by requiring

$$\frac{1}{T_L} \int_0^{T_L} \delta \boldsymbol{x}(\boldsymbol{x}, \tau)\, \mathrm{d}\tau = 0. \quad (2.17)$$

Therefore, the GLM theory associates the Lagrangian mean quantity with the mean location $\boldsymbol{x}$, and $\delta \boldsymbol{x}$ is a fluctuating quantity. The Lagrangian fluctuation velocity is naturally defined as

$$\boldsymbol{u}^l(\boldsymbol{x}, \delta \boldsymbol{x}, t) = \langle \boldsymbol{u} \rangle (\boldsymbol{x} + \delta \boldsymbol{x}(\boldsymbol{x}, t)) - \overline{\boldsymbol{u}}^L. \quad (2.18)$$

Due to the periodicity of the mean flow and the quasi-steadiness in our problem set-up, the GLM depends only on the mean vertical coordinate, i.e. $\overline{\boldsymbol{u}}^L(\boldsymbol{x}, t)$ is reduced to $\overline{\boldsymbol{u}}^L(z)$. The pseudo-momentum $\boldsymbol{p}$ is defined as

$$\mathrm{p}_i = \frac{1}{T_L} \int_0^{T_L} \frac{\partial(\delta x_j)}{\partial x_i} u_j^l\, \mathrm{d}\tau, \quad (2.19)$$

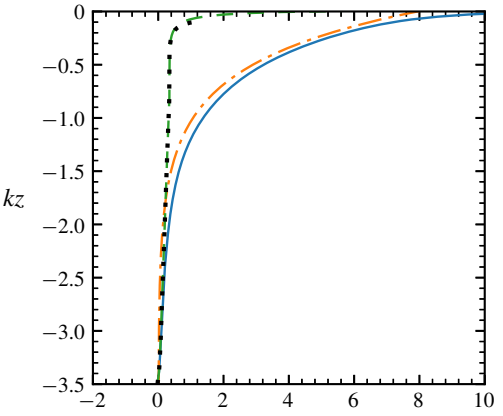

FIGURE 3. (Colour online) Vertical profiles of the different components arising from the wave–current decomposition of case L1: —— $\overline{u}^L$, — · — p_x, −−− u_c and ····· $\langle u\rangle_{xy}$. The $\langle u\rangle_{xy}$ is defined only up to the wave trough, and its profile is close to u_c. Only the x-components are compared because the z-components are negligible. The results are normalized by u_*.

which is contributed by the fluctuating quantities and is thus a property of the oscillatory flow (wave).

We note that, strictly speaking, $\langle \boldsymbol{u}\rangle$ extracted by the phase averaging (2.13) includes the mean current and all spanwise-invariant oscillatory motions that move with the wave phase speed c, and the latter may include turbulence structures that are spanwise uniform and have a convection speed of c. However, in this study, the turbulence motions are much weaker than the wave orbital motions. Therefore, we assume the oscillatory motions $\boldsymbol{u}_w$ obtained from (2.15) are all due to the gravity surface wave. It is also confirmed later in § 4.1 that $\boldsymbol{u}_w$ generally agrees with the velocity of a Stokes wave.

The quasi-Eulerian definition of the current has the advantage of being able to account for the region between wave troughs and crests. By contrast, the Eulerian mean $\langle u\rangle_{xy}$, where $\langle\cdot\rangle_{xy}$ denotes the average over the x–y plane, is well defined up to the wave trough. Leibovich (1980) shows that the Stokes drift $\boldsymbol{u}_s = \overline{\boldsymbol{u}}^L - \langle \boldsymbol{u}\rangle_{xy}$ differs from $\boldsymbol{p}$ by $O(a^3k^3\mathcal{U})$, where $\mathcal{U}$ is the characteristic velocity scale of the current and is $O(u_*)$ as discussed in § 2.4. The difference between the Eulerian mean $\langle u\rangle_{xy}$ and the quasi-Eulerian velocity u_c is also $O(a^3k^3\mathcal{U})$. Therefore, the Eulerian current can be approximated by the quasi-Eulerian current. Figure 3 shows an example of the wave–current decomposition (2.14) and the Eulerian current $\langle u\rangle_{xy}$. In the figure, $\langle u\rangle_{xy}$, which is defined only up to the wave trough, is very close to u_c in the region below the wavy surface. After the above decomposition procedure, the current and wave components are separated, so that we can analyse the effects of waves and current on the turbulence individually. For the shear-driven turbulence with a flat surface, there exists no wave motions or turbulence structures that move as fast as the wave phase speed. Therefore, both $\boldsymbol{p}$ and $\boldsymbol{u}_w$ are zero, and the Lagrangian average is the same as the Eulerian average, i.e. $\overline{u}^L = u_c = \langle u\rangle_{xy}$.

3. Flow features of Langmuir turbulence

The characteristic features of Langmuir turbulence, which are successfully captured in our wave-phase-resolved simulations, are presented and compared with those of the

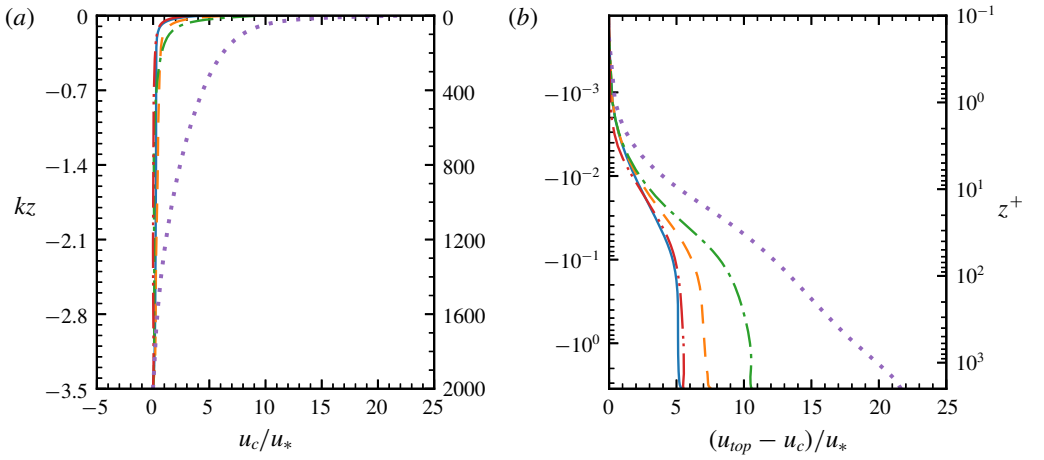

FIGURE 4. (Colour online) Profiles of current velocity u_c for Langmuir turbulent flows in cases L1 (——), L1S (— · · —), L2 (– – –), L3 (— · —) and the shear-driven turbulence case S (· · · · · ·). (*a*) Plots the normalized current velocity u_c/u_*, and (*b*) plots the current using the velocity difference from the surface value, $u_c - u_{top}$. In (*a*), the current velocity in cases L1, L1S and L3 are very close in the bulk region. In both (*a*) and (*b*), two dimensionless vertical coordinates are used, which are kz (left axis) and the viscous units $z^+ = -zu_*/\nu$ (right axis).

shear-driven turbulence in this section. The mean current is first examined in § 3.1. Then, the surface flow structures (windrows) are illustrated in § 3.2. The instantaneous turbulence vortices are shown in § 3.2, where the wave-phase dependency of the turbulence field is observed. In § 3.3, the characteristics of the vortex structures are further examined based on the conditional averaging obtained from the linear stochastic estimation method.

3.1. *Current*

Figure 4(*a*) shows the profiles of the current u_c. For all the wave-forcing cases considered in this study, the current exhibits nearly uniform distribution from the bottom to the near-surface region, indicating that the bulk flow is well mixed vertically. Only in the vicinity of the surface does u_c increase rapidly. On the other hand, the current profile of the shear-driven turbulence in case S has a larger gradient. As a result, the current in the wave-forcing cases is much weaker than the shear-driven current. This well mixed bulk flow when the wave is present is consistent with the feature of strong vortices in Langmuir turbulence, which enhance the vertical fluctuations and thus the mixing significantly (Thorpe 2004; Sullivan & McWilliams 2010).

To show the near-surface behaviour more clearly, figure 4(*b*) plots the profiles of the current using the velocity difference from the surface value, $u_c - u_{top}$, with respect to the distance from the surface in viscous units $z^+ = -zu_*/\nu$ in semi-logarithmic scale. In the shear-driven turbulence (case S), the current profile exhibits a logarithmic region as expected. Applying a least-square fitting of the profile between $z^+ > 30$ and $z/\bar{H} > -0.15$ ($z^+ < 300$), we obtain the von Kármán coefficient $\kappa = 0.39$ and $b = 1.7$ in the logarithmic law of the wall $u/u_* = \kappa^{-1} \ln z^+ + b$. The coefficients

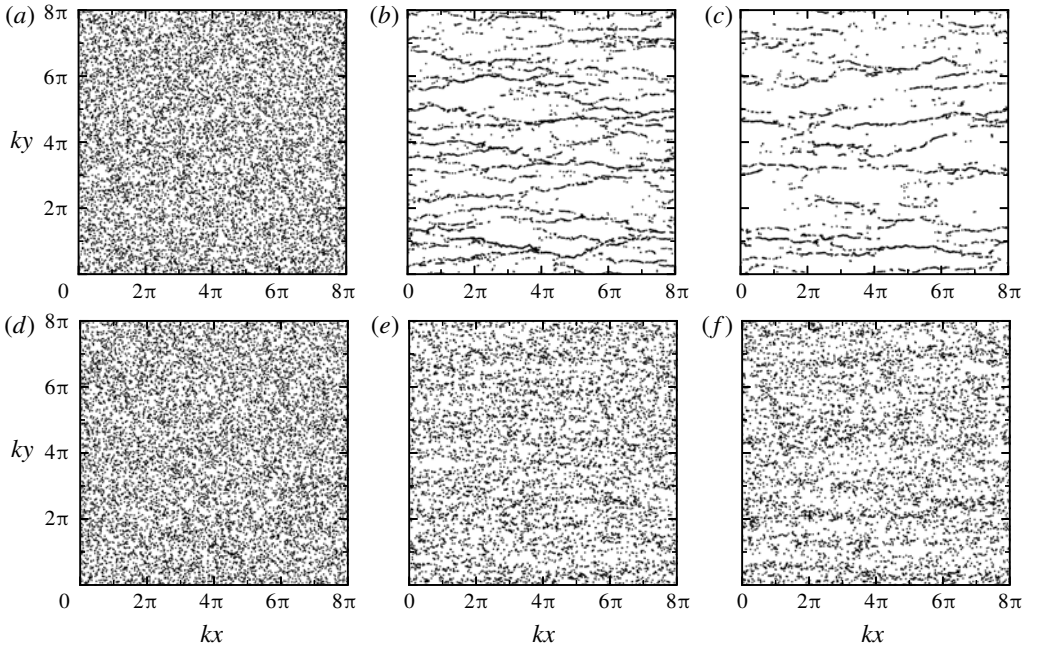

FIGURE 5. Distribution of 10^4 particles after being randomly released on the surface in the (*a–c*) Langmuir turbulence (case L1) and (*d–e*) shear-driven turbulence (case S). (*a,d*) Initial particle distribution at $t = 0$; (*b,e*) at $tu_*/\bar{H} = 0.156$ (100 wave periods after releasing); (*c,f*) at $tu_*/\bar{H} = 0.311$ (200 wave periods after releasing).

are consistent with the direct numerical simulation of shear-driven turbulence in Tsai, Chen & Moeng (2005), where κ was found between 0.35 and 0.4, and b between 1.1 and 1.9. In contrast, when the wave is present, the velocity difference between the top and bottom is significantly reduced. Most of the velocity change occurs in the near-surface region (figure 4*a*), where the viscous effect is significant. The logarithmic region is not obvious in the cases with wave (figure 4*b*). As La_t decreases, the velocity difference also becomes smaller, indicating that the momentum mixing is enhanced by the wave forcing. The uniformity of the current in the bulk flow and the trend of the current profile with La_t observed in the wave-forcing cases are qualitatively consistent with the Langmuir turbulence simulations using the wave-phase-resolved method (Zhou 1999) and the CL equations in the literature (cf. McWilliams *et al.* 1997; Li *et al.* 2005).

3.2. *Instantaneous flow structures*

Langmuir turbulence can lead to distinct surface structures, e.g. windrows. To compare the surface flow structures with or without the wave, we place Lagrangian tracer particles on the surface and track their locations $\boldsymbol{x}$ by integrating $\mathrm{d}\boldsymbol{x}/\mathrm{d}t = \boldsymbol{u}(\boldsymbol{x}, t)|_{z=\eta}$ in time. The results are shown in figure 5. Initially, 10^4 particles are released randomly in the Langmuir turbulence (case L1) and the shear-driven turbulence (case S), as shown in figures 5(*a*) and 5(*d*), respectively. Particles in Langmuir turbulence are quickly aggregated into narrow streamwise streaks (figure 5*b*) and the number of bands decreases with time as they further merge with each other (figure 5*c*). These streaks show 'Y'-shaped merging in the x-direction, as one would observe with the

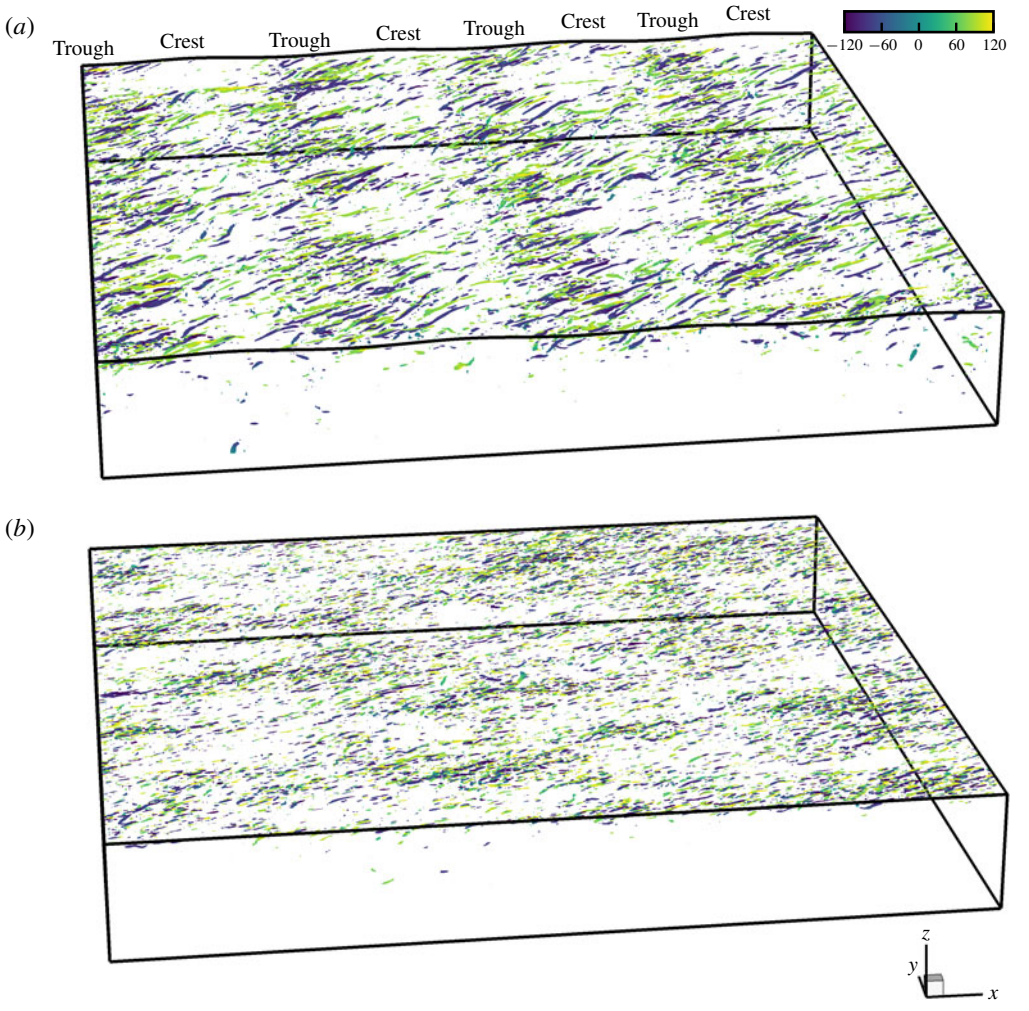

FIGURE 6. (Colour online) Instantaneous vortical structures in the flow fields in (*a*) case L1 ($La_t = 0.35$) and (*b*) case S ($La_t = \infty$). The vortices are educed by the iso-surfaces of $\lambda_2 = -1, 650$. The iso-surfaces are coloured with the contours of ω_x.

windrows (Li & Garrett 1993; Farmer & Li 1995; Melville, Shear & Veron 1998). By contrast, in shear-driven turbulence, the particles are still scattered after the same duration of time as shown in figure 5(*e*,*f*). This is consistent with the literature that Langmuir turbulence is more effective in creating streaks than the shear-driven turbulence (e.g. Teixeira & Belcher 2010).

Figure 6 compares the instantaneous vortices in Langmuir turbulence (case L1) and shear-driven turbulence (case S). The vortical structures are visualized by the iso-surfaces of λ_2, the second largest eigenvalue of the tensor $\boldsymbol{S}^2 + \boldsymbol{\Omega}^2$, with $\boldsymbol{S} = (\nabla \boldsymbol{u} + \nabla \boldsymbol{u}^{\mathrm{T}})/2$ being the strain rate tensor and $\boldsymbol{\Omega} = (\nabla \boldsymbol{u} - \nabla \boldsymbol{u}^{\mathrm{T}})/2$ being the rotation tensor (Jeong & Hussain 1995), widely used for identifying vortices in turbulent flows. The iso-surfaces are coloured by the contours of the streamwise vorticity $\omega_x = \partial w/\partial y - \partial v/\partial z$. Both types of flows are dominated by quasi-streamwise vortices near the surface. However, the vortices in Langmuir turbulence are elongated

and more aligned in the streamwise direction compared with those in shear-driven turbulence, consistent with the results in the literature (McWilliams *et al.* 1997; Teixeira & Belcher 2010). It can also be observed that most vortex tubes in Langmuir turbulence are accompanied by vortices of opposite signs of ω_x, forming counter-rotating vortex pairs, which can induce converging/diverging zones on the surface. The vortex pairs also show a converging trend in the $+x$-direction. This corresponds to the merging of the vortices and the 'Y'-junction of the windrows, which are considered inherent to the wave forcing according to the analyses of the CL equation (Li & Garrett 1993; Bhaskaran & Leibovich 2002; Zhang *et al.* 2015). On the other hand, the vortices in shear-driven turbulence do not seem to appear in pairs.

What is most interesting in figure 6(*a*) is that the vortex distribution exhibits a correlation with the wave phase. Stronger turbulence vortices are located under the wave trough. This indicates that the wave orbital motions have a direct effect on the turbulence, leading to the wave-phase-dependent variation of the turbulence. Such an effect can only be captured in the wave-phase-resolved frame and more in-depth analyses of the wave-phase dependency are provided in § 5.

3.3. *Coherent vortex structure*

The instantaneous flow field only provides a qualitative overview of the vortex structures. A more detailed characterization of the coherent vortex structure can be obtained by a conditional averaging of the flow field based on a vortex identification criterion. Here we use the linear stochastic estimation (LSE) method to obtain the conditional average (Adrian & Moin 1988; Adrian 1994), which is shown to be able to identify coherent turbulence structures, such as the hairpin vortices (Christensen & Adrian 2001). The detailed definition of the LSE of a quantity f, denoted by $\langle f(\boldsymbol{x}')|\Lambda_{ci}(\boldsymbol{x})\rangle$, is given in appendix C. Here, $f(\boldsymbol{x}')$ is a conditional-averaged field around the conditioning event $\Lambda_{ci}(\boldsymbol{x})$, where $\boldsymbol{x}'$ denotes the coordinates relative to the location of the conditioning event. The parameter $\Lambda_{ci}(\boldsymbol{x})$ is a signed swirling strength (Zhou *et al.* 1999; Christensen & Adrian 2001; Wu & Christensen 2006) defined by (C 1), chosen as the conditioning event for the estimation of the vortex structure. The parameter Λ_{ci} contains information of the rotating direction of the streamwise vortices, and we apply the LSE method for $\Lambda_{ci} > 0$ and $\Lambda_{ci} < 0$ separately to avoid the cancellation between vortices of opposite rotating directions. The LSE method has a few features. First, the LSE approximation is based on all instances of $\Lambda_{ci} > 0$ and $\Lambda_{ci} < 0$ and no threshold needs to be determined. Second, the LSE definition (C 2*b*) is closely related to the two-point correlation, therefore the LSE approximated field reflects the statistical correlations of f with the event Λ_{ci} (Adrian 1994). Third, the LSE result is linearly correlated with the value of Λ_{ci}, which means that the characteristics of the extracted structures remain independent of Λ_{ci} and only the magnitude of the LSE field varies with Λ_{ci} (Christensen & Adrian 2001).

Figure 7 shows the conditional-averaged vortex structure obtained from the Langmuir turbulence (case L1) and the shear-driven turbulence (case S). The side views and front views of the vortex structure are shown in figure 8. In the above figures, the same conditioning event, $\Lambda_{ci} = 1$ at $k(z - \eta) = 0.45$, is used for the reconstruction of the flow field for the comparison between the two types of flows. We note here that the averaged field with $\Lambda_{ci} < 0$ is the mirror of that with $\Lambda_{ci} > 0$ about the axis $y' = 0$. Due to the reflection symmetry, we only discuss the conditional-averaged field with positive Λ_{ci}.

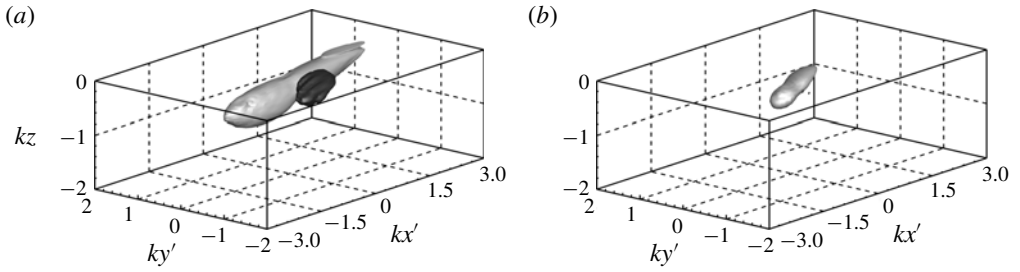

FIGURE 7. Conditional-averaged vortex structure extracted by the linear stochastic estimation with $\Lambda_{ci} = 1$. The vortices are identified by the iso-surfaces of $\langle\omega_x|\Lambda_{ci}\rangle = 0.07ku_*$ (light grey) and $\langle\omega_x|\Lambda_{ci}\rangle = -0.07ku_*$ (dark grey). (*a*) Vortex structure in the Langmuir turbulence $La_t = 0.35$ (case L1). (*b*) Vortex structure in the shear-driven turbulence $La_t = \infty$ (case S).

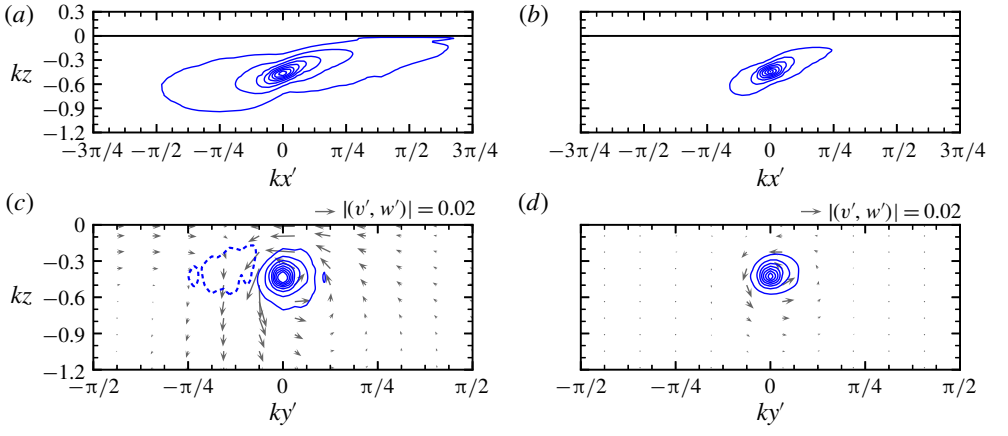

FIGURE 8. (Colour online) The side views and front views of the conditional-averaged vortex structure in Langmuir turbulence $La_t = 0.35$ (case L1) and shear-driven turbulence with $La_t = \infty$ (case S): (*a*) and (*b*) show the structure in the Langmuir turbulence; (*c*) and (*d*) show the vortex structure in the shear-driven turbulence; (*a*) and (*c*) show the side views of the contours of $\langle\omega_x|\Lambda_{ci}\rangle$ in the plane $y' = 0$; (*b*) and (*d*) show the front views of the contours of $\langle\omega_x|\Lambda_{ci}\rangle$ and the vectors of $(\langle v'|\Lambda_{ci}\rangle, \langle w'|\Lambda_{ci}\rangle)$ in the plane $x' = 0$. The positive contours start with $0.02ku_*$ in an increment of $0.04ku_*$ and the negative contours start with $-0.02ku_*$ in an increment of $-0.04ku_*$. The conditions are the same as figure 7.

As shown in figures 7 and 8, the vortices in both types of flows are quasi-streamwise vortices that extend in the downwind direction and tilt upward towards the surface, but the length scale and the structures are different. The streamwise extension of the vortex tube in Langmuir turbulence (case L1) is approximately eight times the spanwise width, as shown in figure 8(*a,b*). On the other hand, in shear-driven turbulence, the streamwise length is much shorter, only approximately three times the width (figure 8*c,d*). These features are consistent with our observations from the instantaneous field (figure 6) where vortices are more elongated in the Langmuir turbulence than in the shear-driven turbulence. Moreover, in the Langmuir turbulence, a counter-rotating vortex appears on the $-y$ side of the central vortex of $\Lambda_{ci} > 0$, but barely exists in the shear-driven turbulence. This implies that there

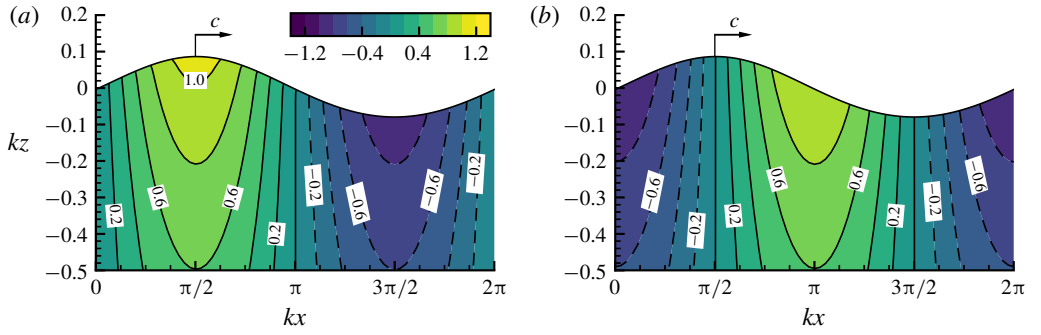

FIGURE 9. (Colour online) Contours of wave velocity (*a*) u_w, (*b*) w_w for case L1. Negative contours are denoted by dashed lines. The results are normalized by $a\omega$.

is a higher probability that counter-rotating vortices appear side by side in pairs in Langmuir turbulence than in shear-driven turbulence. Figure 8(*b*) also shows that the counter-rotating vortex pair induces a strong downwelling motion between the two vortices and a convergence zone exists above, consistent with the enhanced vertical mixing and surface convergence in Langmuir turbulence.

We have so far illustrated the current profiles and turbulence vortex structures from our wave-phase-resolved simulations, which all show distinct features of Langmuir turbulence. Specifically, we have observed in the instantaneous field (figure 6) that the vortex distribution is wave-phase dependent, which is further examined and explained in § 5. The effect of the wave-phase variation of the vorticity on the generation of the elongated vortices in Langmuir turbulence is discussed in § 6.

4. Wave field

Before we discuss the vorticity distortion in the Langmuir turbulence (§§ 5 and 6), we need to examine the properties of the wave field in this section. These properties are essential to the understanding of the wave effects in the vorticity dynamics. We first discuss the wave orbital velocity and the resulting orbital straining in § 4.1. Then, the Lagrangian-averaged wave straining is analysed in § 4.2, which is related to the cumulative effect of the wave on turbulence. Here, only case L1 is presented because, as discussed below, the features of the wave field of other cases are similar.

4.1. *Eulerian properties of wave*

The contours of wave orbital velocity u_w and w_w in case L1 are shown in figures 9(*a*) and 9(*b*), respectively. The wave elevation and the velocity distribution in general agree with those of Stokes wave, which also holds for other cases (L2-L3 and L1S). The turbulence-induced surface fluctuation, $\eta' = \eta - \langle\eta\rangle$, is found to be negligibly small. Among all the cases in this study, the root mean squared turbulence surface fluctuation η'_{rms} is less than 1.2 % of the wave amplitude, indicating that the turbulence is relatively weak compared to the surface wave. As expected from Stokes wave, u_w is positive and negative under the wave crest and trough, respectively. The w_w is positive under the forward slope, and negative under the backward slope. The two components of the wave velocity vary sinusoidally with the wave phase and form an orbital motion. In the vertical direction, the velocity magnitude decays exponentially with the depth.

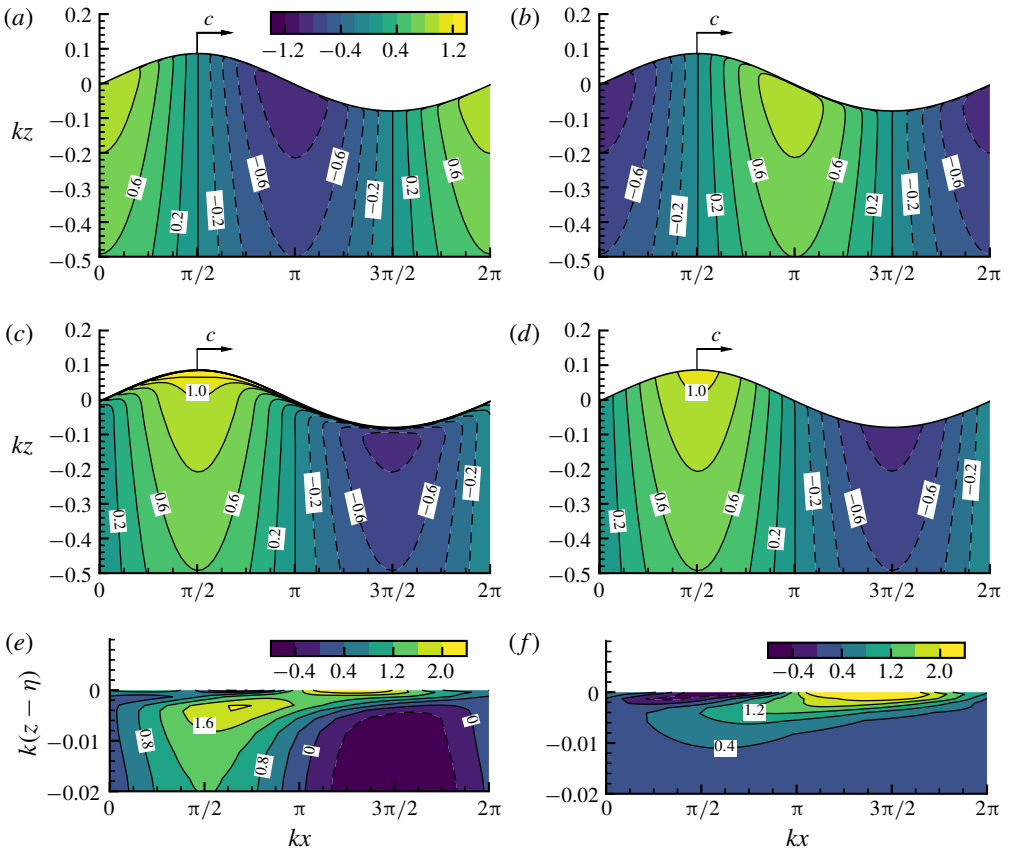

FIGURE 10. (Colour online) Contours of wave strain rate (*a*) $\partial u_w/\partial x$, (*b*) $\partial w_w/\partial z$, (*c*) $\partial u_w/\partial z$ and (*d*) $\partial w_w/\partial x$ for case L1. (*e*) A close-up view of the near-surface region of (*c*). (*f*) The vorticity $\partial u_w/\partial z - \partial w_w/\partial x$ in the near-surface region. The results are normalized by $ak\omega$.

It is worth mentioning that, when the frame translates with the wave phase speed c such that the wave phase is fixed, fluid particles are convected in the opposite direction to the wave propagation, i.e. the $-x$-direction in the wave-following frame. In other words, the wave propagates over a particle in a cyclic order of trough, forward slope, crest and backward slope. The perspective of the convection direction of fluid particles in a wave-following frame is important because the following analyses of the vorticity dynamics of the wave–turbulence interactions are performed within this frame.

The horizontally and vertically varying orbital velocity results in a straining field that also varies with the wave phase and the depth, as shown in figure 10. We first look at the normal gradients. The streamwise normal gradient $\partial u_w/\partial x$ (figure 10*a*) is positive under the backward slope and negative under the forward slope. The vertical normal gradient (figure 10*b*) satisfies $\partial w_w/\partial z = -\partial u_w/\partial x$. Therefore, fluid elements experience stretching in the x-direction and compression in the z-direction under the backward slope, and the opposite process occurs under the forward slope.

The gradients $\partial u_w/\partial z$ and $\partial w_w/\partial x$ (figure 10*c*,*d*) represent the shear deformations of fluid elements. The value of $\partial w_w/\partial x$ is positive under the crest and negative under the trough. The distribution of $\partial u_w/\partial z$ (figure 10*c*) shows a two-layer structure that

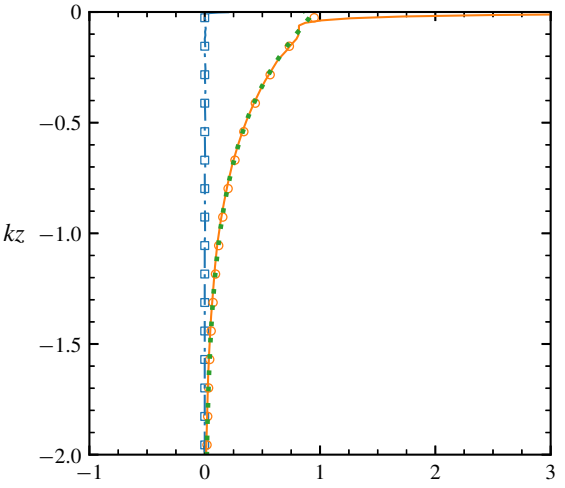

FIGURE 11. (Colour online) The profiles of the Lagrangian mean wave velocity gradients: $\overline{\partial u_w/\partial x}^L = -\overline{\partial w_w/\partial z}^L$ (— · —), $\overline{\partial u_w/\partial z}^L$ (——), $\overline{\partial w_w/\partial x}^L$ (· · · · · ·) from our simulation and $\overline{\partial u_w/\partial x}^L$ (□), $\overline{\partial u_w/\partial z}^L$ (○) based on the fifth-order Stokes wave theory (Fenton 1985). Case L1 is shown here and the results are normalized by $a^2k^2\omega$. Note that the numerical results of $\overline{\partial u_w/\partial x}^L$ ($-\overline{\partial w_w/\partial z}^L$) and the theoretical result of $\overline{\partial u_w/\partial x}^L$ are very close to each other; and the numerical results of $\overline{\partial u_w/\partial z}^L$ and $\overline{\partial w_w/\partial x}^L$ and the theoretical result of $\overline{\partial u_w/\partial z}^L$ are also indistinguishable from each other.

is not present in the other gradients. In most of the region away from the surface, $\partial u_w/\partial z$ is almost equal to $\partial w_w/\partial z$, i.e. the mean vorticity $\partial u_w/\partial z - \partial w_w/\partial x$, which is in the spanwise direction, is essentially zero and the wave field is irrotational. As the surface is approached, $\partial u_w/\partial z$ changes drastically. The near-surface behaviour of $\partial u_w/\partial z$ is shown with respect to the distance from the surface $(z-\eta)$ in figure 10(*e*). The thickness of the layer where the drastic change occurs is of the same order as the thickness of the Stokes layer, $\delta_S = (2\nu/\omega)^{1/2}$, whose dimensionless value is $k\delta_S = 0.0017$ in this case. This layer is associated with the viscous effect. The near-surface change of $\partial u_w/\partial z$ corresponds to a layer of non-zero mean vorticity that deviates from the irrotational wave solution, as shown in figure 10(*f*). The viscous layer is so thin that its contribution to the overall dynamics of the wave–turbulence interaction is small. In most of the region, $\partial u_w/\partial z$ and $\partial w_w/\partial x$ impose an irrotational shearing distortion effect on fluid elements.

4.2. *Lagrangian properties of wave*

Next, we discuss the Lagrangian average of the wave straining, which is important to the long-term vorticity dynamics analysed in § 6. Applying the Lagrangian average $\overline{(\cdot)}^L$ (2.16) to the wave orbital velocity gradients (figure 10*a–d*), we obtain the Lagrangian velocity gradients of the wave, $\overline{\partial u_w/\partial x}^L$, $\overline{\partial w_w/\partial z}^L$, $\overline{\partial u_w/\partial z}^L$ and $\overline{\partial w_w/\partial x}^L$, which represent the cumulative straining applied by the wave on fluid elements over a Lagrangian period. The vertical profiles of the above Lagrangian velocity gradients are shown in figure 11. Only case L1 is shown due to the similarity in the wave field among different cases as pointed out in § 4.1.

We first look at the normal gradients, $\overline{\partial u_w/\partial x}^L$ and $\overline{\partial w_w/\partial z}^L$. Both are nearly zero, indicating that the cumulative stretching applied on fluid elements over a Lagrangian period is negligible. The trajectories of the fluid particles are symmetric about the two sides of the wave crest and trough, while $\partial u_w/\partial x$ (or $\partial w_w/\partial z$) is anti-symmetric (figure 10*a,d*), therefore the normal straining that the fluid elements experience under the forward slope is cancelled by that under the backward slope.

On the other hand, the Lagrangian shear straining, $\overline{\partial u_w/\partial z}^L$ and $\overline{\partial w_w/\partial x}^L$, has positive values with a magnitude of $O(a^2k^2\omega)$. This indicates that, over a Lagrangian period, the wave imposes a net shearing distortion on fluid elements. This is mostly due to the difference in the shear strain rate between under the wave crest and under the trough, and the different convection times under the wave crest and trough. As shown in figures 10(*c*) and 10(*d*), the magnitudes of $\partial u_w/\partial z$ and $\partial w_w/\partial x$ outside of the viscous layer increase with z. Because the trajectories of the particles roughly follow the surface geometry, the positive straining on the fluid particles when they are under the crest is larger than the negative straining under the trough. Therefore, the net Lagrangian shear straining is positive. Note that the effect of the viscous boundary layer is also manifested in the sharp increase of $\overline{\partial u_w/\partial z}^L$ in the vicinity of the surface. However, in most of the region away from the surface, $\overline{\partial u_w/\partial z}^L \approx \overline{\partial w_w/\partial x}^L$ is satisfied due to the irrotationality of the wave flow as discussed in § 4.1.

The theoretical Lagrangian mean of wave velocity gradients based on the fifth-order irrotational wave theory of Fenton (1985) is also shown in figure 11. It can be seen that the Lagrangian velocity gradients from the present simulations agree well with the theoretical prediction outside the surface viscous layer, indicating that the irrotational wave solution is a good approximation of the wave field. The effect of the surface viscous layer, the thickness of which scales with $(2\nu/\omega)^{1/2}$, should diminish with a decreasing ν (increasing Reynolds number $Re_\tau = u_* H/\nu$). The agreement with the irrotational wave solution is expected, because the current and turbulence are weak and cannot lead to a significant modification of the wave kinematics (Magnaudet & Thais 1995; Ardhuin, Rascle & Belibassakis 2008). We shall note that, when the strong current or turbulence is present or the wave is short, the waves can become rotational (Craik 1982; Phillips & Wu 1994; Veron & Melville 2001; Gutiérrez & Aumaître 2016). Under such conditions, the coupled wave–current–turbulence evolution is more complex and can be studied using the wave-phase-resolved simulation in the future.

The Eulerian and Lagrangian effects of the wave on fluid elements are summarized in figure 12. In the Eulerian frame, the wave orbital straining varies periodically with the wave phase. Under the wave forward slope, fluid elements are compressed in the x-direction and stretched in the z-direction. The opposite occurs when the fluid elements are under the backward slope. The wave also applies an irrotational shearing that distorts the fluid elements, and the distortion effect is opposite under the crest and trough. In § 5 below, the effects of the periodically varying straining on the turbulence vortices underneath are analysed. As for the Lagrangian straining, although one order of magnitude smaller than the orbital straining, the net shear straining on the fluid elements can lead to cumulative distortion of the fluid elements. The cumulative effect on the vorticity dynamics in Langmuir turbulence is discussed in detail in § 6.

5. Variation of vortex structures and statistics with wave phase

In § 3.2, the instantaneous vorticity field (figure 6) indicates that there exists a correlation between the vortex structure and the wave phase. In this section, we perform detailed statistical analyses of the turbulence vortex structure and vorticity

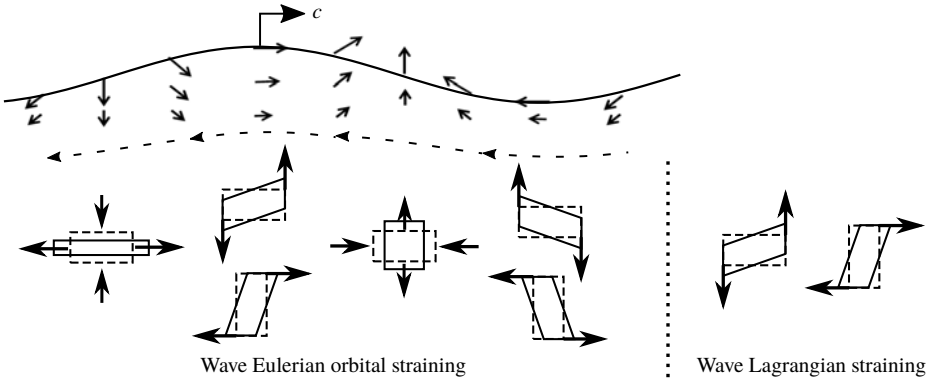

FIGURE 12. Sketch of the effects of wave Eulerian orbital straining and Lagrangian straining on fluid elements. The arrows along the dashed line indicate the convection direction of the fluid elements relative to the wave phase. The original fluid elements are denoted by dashed rectangles, and the fluid elements distorted by the wave straining are denoted by solid rectangles.

fluctuations in the wave-phase-resolved frame and examine the wave-phase variation of the turbulence vorticity. The wave-phase dependency is examined in three aspects, the LSE analysis of the vortex structure (§ 5.1), vorticity enstrophy (§ 5.2) and vorticity inclination angle (§ 5.3). Then, in § 5.4, the vorticity evolution equation is evaluated with the wave-phase resolved to explain the mechanism for the phase variation of the vorticity.

5.1. *Variation of vortex structure*

The coherent vortex structure under different wave phases is obtained through the LSE method described in § 3.3. It is found that the variation of the vortex structure is more prominent in the x–z plane, therefore the side views of the vortex obtained from the Langmuir case L1 are plotted in figure 13. Only the flow structure associated with $\Lambda_{ci} > 0$ is discussed below, because the flow fields corresponding to positively and negatively rotating vortices are in reflection symmetry about $y' = 0$.

As shown in figure 13, the characteristics of the quasi-streamwise counter-rotating vortices vary with the wave phase. The difference is mainly manifested in the vortex length and the inclination angle in the x–z plane. The dash-dotted line in figure 13 marks the streamwise extension and the inclination angle of the contour level $\langle \omega_x | \Lambda_{ci} \rangle = 0.06 k u_*$. This level is chosen because it is relatively localized under each phase.

We first discuss the length of the vortex. The vortex under the wave trough (figure 13*d*) is longer than under the crest (figure 13*b*), indicating that the vortices under the trough are stronger than those under the crest. This is consistent with our observations of the instantaneous vortex field (figure 6*a*), where stronger vortices are located under the trough. Because the vortex is convected in the $-x$-direction relative to the wave, the variation of the vortex length indicates that the vortex strength weakens under the forward slope as the wave phase changes from the trough to crest. The opposite process occurs under the backward slope.

In addition to the vortex length, the inclination of the vortex also varies with the wave phase. Under the wave crest, i.e. when the vortex is convected from under the forward slope to under the backward slope, the vortex is tilted towards the

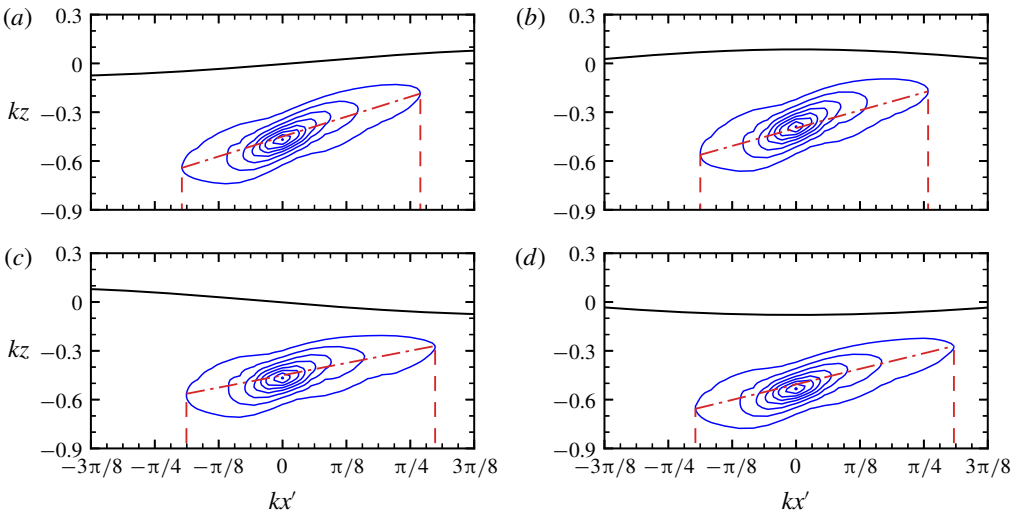

FIGURE 13. (Colour online) Conditional-averaged vortex structure in Langmuir turbulence with $La_t = 0.35$ (case L1) under (*a*) the backward slope, (*b*) the crest, (*c*) the forward slope and (*d*) the trough. The vortex structure is elucidated by the contours of $\langle \omega_x | \Lambda_{ci} \rangle$ in the plane $y' = 0$. The positive contours start with $0.06ku_*$ in an increment of $0.04ku_*$. The dash-dotted lines (— · —) connect the two ends of the contour level $0.06ku_*$, and the vertical dashed lines (– – –) mark the streamwise location of the two ends of the dash-dotted lines.

Case	Mean	Forward slope		Backward slope		Difference
	ϕ_m	ϕ_f,	$\phi_f - \phi_m$	ϕ_b,	$\phi_b - \phi_m$	$\phi_b - \phi_f$
L1	14.4	10.9,	−3.5	17.3,	2.9	6.4
L1S	13.4	6.8,	−6.6	18.9,	5.5	12.1
L2	14.6	11.3,	−3.3	17.5,	2.9	6.2
L3	25.1	21.7,	−3.4	27.8,	2.7	6.1

TABLE 2. The values of the inclination angle (in degree), the angle between the x-axis and the dash-dotted line (— · —) in figure 13, of the conditional-averaged vortex structure for different cases. The second column shows the mean vortex angles of different wave phases ϕ_m. The third column shows the vortex angles under wave forward slope ϕ_f and their deviation from the mean angles $\phi_f - \phi_m$. The fourth column show the vortex angles under the backward slope ϕ_b and their deviation from the mean angles $\phi_b - \phi_m$. The forward slope and backward slope correspond to the locations of minimum and maximum tilting, respectively. The last column shows the difference in the vortex angle between the minimum and maximum tilting.

vertical direction. The tilting direction reverses under the wave trough. Therefore, the variation of vortex angle roughly follows the slope of the wave surface and the maximum and minimum tilting occurs under the backward and forward slope, respectively. Table 2 presents the mean, maximum and minimum angles of the vortex for the different Langmuir turbulence cases. Among the cases L1, L2 and L3, where the wave steepness is the same, the amplitude of the vortex angle fluctuation and the deviation of the maximum and minimum tilting angles from the mean angle

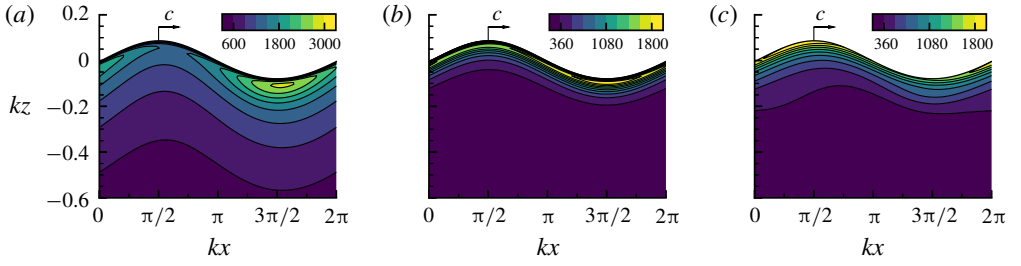

FIGURE 14. (Colour online) Contours of phase-averaged enstrophy components for case L1: (*a*) $\langle\omega_x^2\rangle$; (*b*) $\langle\omega_y'^2\rangle$; (*c*) $\langle\omega_z^2\rangle$. The enstrophy is normalized by $(ku_*)^2$.

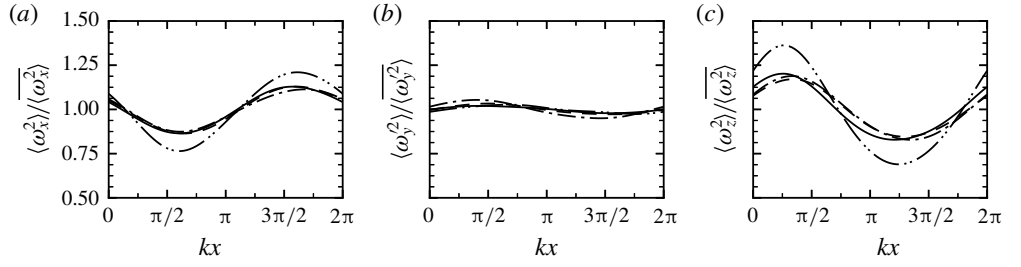

FIGURE 15. Normalized variation of enstrophy components with the wave phase, (*a*) $\langle\omega_x^2\rangle/\overline{\langle\omega_x^2\rangle}$, (*b*) $\langle\omega_y'^2\rangle/\overline{\langle\omega_y'^2\rangle}$ and (*c*) $\langle\omega_z^2\rangle/\overline{\langle\omega_z^2\rangle}$, at depth $k(z-\eta)=-0.2$ for case L1 (——), case L2 (– – –), case L3 (— · —) and case L1S (— · · —).

are roughly the same. This indicates that the mechanism of the vortex tilting is the same. The maximum and minimum tilting angles are slightly asymmetric about the mean angle, indicating that the forward and backward tilting rates are different. For case L1S with a larger wave steepness, the difference between the maximum and minimum angle is much larger. This indicates that the amplitude of the vortex tilting fluctuations is affected by the wave steepness, which is expected.

In summary, figure 13 gives an overall view of the wave-phase-dependent oscillation of the vortices underneath a propagating surface wave. The vortices are elongated and compressed periodically as the wave passes. Meanwhile, the tilting angle of the vortices also fluctuates with the wave phase. It should be noted here that the variation of the vortex structure lies in the change of the turbulence vorticity field. Therefore, the vorticity statistics are examined below.

5.2. *Variation of enstrophy*

The enstrophy indicates the intensity of vorticity fluctuations. The near-surface distribution of the enstrophy within the wave-phase-resolved frame is shown in figure 14 for the Langmuir turbulence case L1. Figure 15 shows the relative variation of the enstrophy at a constant distance from the surface for the different Langmuir turbulence cases. For the spanwise component, the turbulence vorticity ω_y' is used, i.e. the mean-flow-induced vorticity $\langle\omega_y\rangle$ is subtracted from the total vorticity ω_y.

As expected, the streamwise vorticity is dominant, because the vortical structures observed in §§ 3.2 and 3.3 are streamwise oriented mostly. The streamwise enstrophy also shows a strong dependence on the wave phase. Both figures 14 and 15 show that the maximum and minimum of $\langle\omega_x^2\rangle$ occur roughly under the trough and under

the crest, respectively. This is also consistent with the variation of the vortex length (figure 13), indicating that the elongation and compression of the vortices are related to the variation of ω_x. It should be pointed out that the locations of maximum and minimum $\langle\omega_x^2\rangle$, as shown in figure 15, are actually slightly ahead of the trough and crest, respectively, for which the reason is explained later in § 5.4.

Compared with $\langle\omega_x^2\rangle$, $\langle\omega_y'^2\rangle$ (figure 14*b*) is weaker and more concentrated near the surface, therefore the turbulence vortices are mostly tilted in the x–z plane. The contour lines of $\langle\omega_y'^2\rangle$ follow the surface geometry, indicating that the dependence of spanwise vorticity fluctuations on the wave phase is weak, which is confirmed by figure 15(*b*).

Figure 14(*c*) shows the distribution of the vertical enstrophy $\langle\omega_z^2\rangle$. The contour lines of $\langle\omega_z^2\rangle$ are shifted compared with the surface shape, indicating that the vertical vorticity fluctuations are modulated by the wave. Figure 15(*c*) shows that high intensity of $\langle\omega_z^2\rangle$ occurs under the backward slope and behind the crest. The value of $\langle\omega_z^2\rangle$ reaches minimum under the forward slope, right after the wave trough passes. Teixeira & Belcher (2002) pointed out that the amplification of the vertical vorticity should be associated with an increase in the streamwise turbulence velocity fluctuations. Therefore, the increase in the vertical vorticity leads to a maximum streamwise Reynolds normal stress slightly behind the crest, which is consistent with the observations of Veron *et al.* (2009) and our results (not plotted).

Comparing the variation of the enstrophy among the different cases in figure 15, we can see that the maximum and minimum phases are similar. However, the relative amplitude of the wave-phase-dependent fluctuations of $\langle\omega_x^2\rangle$ and $\langle\omega_z^2\rangle$ in case L1S is larger than the other cases, indicating that the modulation effect of the wave on the vorticity increases with wave steepness.

5.3. *Variation of inclination angle of vorticity vectors*

The tilting of the vortex structures indicates variations in the orientation of the local vorticity vectors. Following Moin & Kim (1985), Kida & Tanaka (1994) and Guo & Shen (2013), we analyse the statistical distribution of the vorticity inclination angles. Here, we focus on the inclination angle between the x-axis and the projection of $\boldsymbol{\omega}$ onto the x–z plane, i.e.

$$\theta_{xz} = \arctan\left(\frac{\omega_z}{\omega_x}\right), \tag{5.1}$$

because most vortices are vertically slanted in the x–z plane and their spanwise tilting is negligible. The histograms of θ_{xz} under different wave phases are shown in figure 16. Here, the statistics of θ_{xz} are weighted by the vorticity magnitude $\omega_x^2+\omega_z^2$ to highlight the contributions from strong vortices. The statistics reflect the properties of the local vorticity vectors under specific wave phases, which are related to but different from the vortex structures analysed in § 5.1. The vortices are three-dimensional structures and thus are related to vorticity distribution at different phases and depth. As shown in figure 16, the histograms have two peaks, located symmetrically in the first and third quadrants, corresponding to positive and negative vorticity, respectively. The peak locations indicate that the vorticity vectors are mostly inclined at a small angle to the $+x$-axis, consistent with the orientation of the vortical structures shown in preceding sections.

The peaks of the distributions of θ_{xz} (figure 16) vary with the wave phase. Peak θ_{xz} reaches minimum under the forward slope, and increases as the wave passes by until it reaches maximum under the backward slope. After the backward slope passes by,

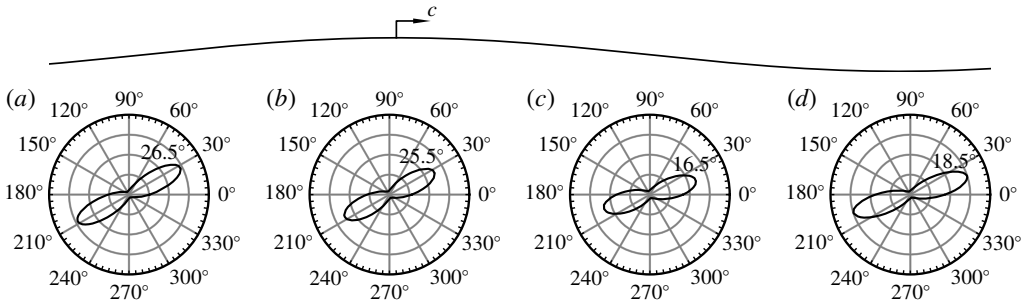

FIGURE 16. Histograms of the statistics of vorticity inclination angle θ_{xz} under: (*a*) backward slope; (*b*) crest; (*c*) forward slope; (*d*) trough. The statistics are taken at $k(z-\eta)=-0.2$ below the surface from case L1. The histograms are weighted by the vorticity magnitude $\omega_x^2+\omega_z^2$. The azimuthal direction corresponds to θ_{xz}, while the radial direction corresponds to the weighted frequency of occurrence.

the opposite process occurs, i.e. θ_{xz} decreases until the vortices are under the forward slope. The fluctuations of the vorticity angle θ_{xz} agree with the vortex tilting direction discussed in § 5.1. The differences between the maximum and minimum θ_{xz} are 10°, 9.5°, 10.5° and 18° for cases L1, L2, L3 and L1S, respectively. This also agrees with the result in § 5.1 that the amplitude of the vortex angle fluctuation mainly depends on the wave steepness. We note that the values of θ_{xz} are larger than the vortex angles presented in table 2. This is because the conditional averaging in § 5.1 samples the flow around the chosen location and the coherent vortex structures are associated with the vorticity at different phases and depth. Take figure 13(*a*) (backward slope) as an example, the two ends of the vortex extend towards the wave crest and trough, respectively, where the vorticity angles decrease. The inner contours, which are more closely related to local vorticity vectors, have larger angles, consistent with the observations in this section.

In §§ 5.2 and 5.3, we have examined the statistical distribution of the vorticity field under different wave phases. The fluctuations of the vorticity statistics, i.e. the enstrophy and the inclination angles, are qualitatively consistent the variation of the coherent vortex structure obtained from the LSE method in § 5.1. This indicates that the physical mechanisms for the variation of the vortex structures are related to the vorticity dynamics. Next, we evaluate the vorticity evolution equations in the wave-phase-resolved frame to illustrate the mechanisms for the wave-phase modulation of the vorticity.

5.4. *Effects of wave straining on variation of vorticity*

In this section, we focus on the evolution of streamwise vorticity ω_x and vertical vorticity ω_z because the components of turbulence vorticity in these two directions are more prominent. The evolution of ω_x and ω_z is described by the vorticity equations

$$\frac{\mathrm{D}\omega_x}{\mathrm{D}t} = \underbrace{\omega_x\frac{\partial u_c}{\partial x}+\omega_z\frac{\partial u_c}{\partial z}}_{\mathcal{D}_x^c}+\underbrace{\omega_x\frac{\partial u_w}{\partial x}+\omega_z\frac{\partial u_w}{\partial z}}_{\mathcal{D}_x^w}+\underbrace{\omega_x\frac{\partial u'}{\partial x}+\omega_y\frac{\partial u'}{\partial y}+\omega_z\frac{\partial u'}{\partial z}}_{\mathcal{D}_x^t}$$
$$\underbrace{-u'\frac{\partial \omega_x}{\partial x}-v'\frac{\partial \omega_x}{\partial y}-w'\frac{\partial \omega_x}{\partial z}}_{\mathcal{T}_x^t}\underbrace{+\nu\nabla^2\omega_x-[\boldsymbol{\nabla}\times(\boldsymbol{\nabla}\cdot\boldsymbol{\tau})]_x}_{\mathcal{F}_x}, \tag{5.2}$$

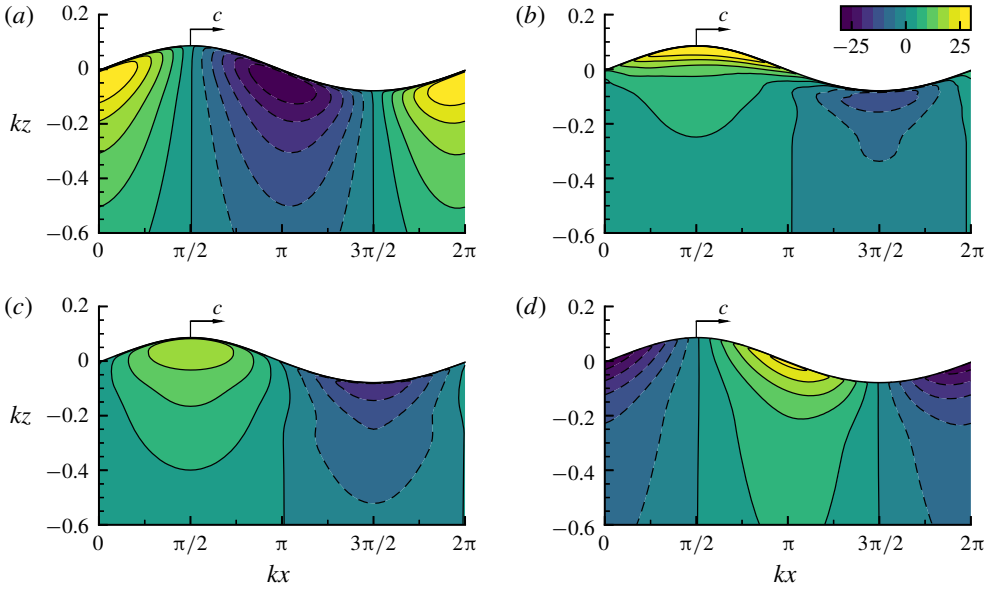

FIGURE 17. (Colour online) Contours of the terms of the wave distortion $\mathcal{D}^w$: (*a*) $\langle\omega_x\partial u_w/\partial x\rangle$, (*b*) $\langle\omega_z\partial u_w/\partial z\rangle$, (*c*) $\langle\omega_x\partial w_w/\partial x\rangle$, and (*d*) $\langle\omega_z\partial w_w/\partial z\rangle$.

$$\frac{\mathrm{D}\omega_z}{\mathrm{D}t} = \underbrace{\omega_x\frac{\partial w_w}{\partial x}+\omega_z\frac{\partial w_w}{\partial z}}_{\mathcal{D}^w_z}\underbrace{+\omega_x\frac{\partial w'}{\partial x}+\omega_y\frac{\partial w'}{\partial y}+\omega_z\frac{\partial w'}{\partial z}}_{\mathcal{D}^t_z}$$
$$\underbrace{-u'\frac{\partial\omega_z}{\partial x}-v'\frac{\partial\omega_z}{\partial y}-w'\frac{\partial\omega_z}{\partial z}}_{\mathcal{T}^t_z}\underbrace{+\nu\nabla^2\omega_z-[\boldsymbol{\nabla}\times(\boldsymbol{\nabla}\cdot\boldsymbol{\tau})]_z}_{\mathcal{F}_z}. \tag{5.3}$$

Here, the material derivative is defined based on the mean velocity, $\mathrm{D}(\cdot)/\mathrm{D}t = \partial(\cdot)/\partial t + \langle\boldsymbol{u}\rangle\cdot\boldsymbol{\nabla}(\cdot)$; $\mathcal{D}^c$, $\mathcal{D}^w$ and $\mathcal{D}^t$ denote the terms representing the distortion (stretching and tilting) on the vorticity by the current, wave and turbulence, respectively; the terms denoted by $\mathcal{T}^t$ are the turbulence transport of the vorticity; and $\mathcal{F}$ represents the forcing due to the viscous force and the SGS stress; the subscripts 'x' and 'z' denote the x and z components of the corresponding terms, respectively. To avoid the cancellation between positive and negative vorticity, the terms in (5.2)–(5.3) are computed using a sign-based conditional phase averaging (Guo & Shen 2013), where we multiply each equation with a sign function of the corresponding vorticity component, sign (ω_i), before applying the phase averaging (2.13). We find that the root mean squared values of $\mathcal{D}^w$ along the x-direction are at least 20 times larger than other terms. This indicates that the wave distortion $\mathcal{D}^w$ is dominant, i.e. the wave-phase-variation of the vorticity statistics is the result of the wave orbital straining. The contours of different terms of $\mathcal{D}^w$ are shown in figure 17. Here, we continue to use case L1 as the representative case for discussion.

We first discuss the variation of the streamwise vorticity due to the wave distortion, which is contributed by two terms, $\omega_x\partial u_w/\partial x$ and $\omega_z\partial u_w/\partial z$, plotted in figures 17(*a*)

and 17(*b*), respectively. The former is dominant, which means that the variation of the streamwise vorticity mainly results from the streamwise stretching of the vortex filaments by $\partial u_w/\partial x$. As shown in figure 17(*a*), under the backward slope, $\omega_x \partial u_x/\partial x$ is positive, indicating that ω_x increases. This is due to the stretching of the vortices in the x-direction by the positive $\partial u_w/\partial x$ (plotted in figure 10*a*). The opposite process occurs under the backward slope. Because the vorticity convection is in the $-x$-direction in the frame moving with the wave, the accumulative effect of the alternating stretching and compression results in maximum ω_x under the wave trough and minimum under the crest. The effect of stretching on ω_x is consistent with the variation of the streamwise component of the enstrophy discussed in § 5.2.

The other term $\omega_z \partial u_w/\partial z$, shown in figure 17(*b*), represents the change of the streamwise vorticity ω_x by the tilting of vortex filaments. Under the crest, the term is positive, indicating that ω_x is generated by the tilting of the vertical vortex filaments. Under the trough, the tilting reverses and weakens ω_x. The tilting effect is weaker than the aforementioned stretching effect, and hence only results in a forward phase shift of the peaks of the streamwise vorticity, which explains the distribution shown in figure 15(*a*). Although the tilting-induced variation of ω_x does not significantly affect the phase distribution of ω_x, it can affect the long-term vorticity evolution when interacting with the wave orbital straining, as discussed later in § 6.3.

Next, we examine the tilting effect $\omega_x \partial w_w/\partial x$ (figure 17*c*) and the stretching effect $\omega_z \partial w_w/\partial z$ (figure 17*d*) on the variation of the vertical vorticity ω_z. The tilting effect is positive under the crest and negative under the trough, indicating that the streamwise vortex filaments are tilted towards the vertical direction under the crest and tilted back under the trough. In general, the tilting direction is consistent with the variation of the vortex structure (§ 5.1) and the inclination angle of the vorticity (§ 5.3), because the flow is dominated by quasi-streamwise vortices and the apparent tilting of the vortices are mainly associated with the tilting of the streamwise vortex filaments.

The stretching and compression of ω_z (figure 17*d*) is related to the normal wave orbital straining $\partial w_w/\partial z$ (figure 10*b*). Under the forward slope, the wave stretches the vortex filaments in the z-direction, which increases ω_z. Under the backward slope, the compression of the filaments decreases ω_z.

The stretching and tilting effects have similar magnitudes, therefore both affect the strength of ω_z. The stretching-induced variation of ω_z leads to a maximum (minimum) ω_z under the crest (trough), while the tilting-induced ω_z leads to a maximum (minimum) ω_z under the backward (forward) slope. Therefore, the maximum of the vertical component of the enstrophy is reached between the crest ($kx = \pi/2$) and the backward slope ($kx = 0$) due to the combined effects of the stretching and tilting, as shown in figure 15(*c*). Correspondingly, the minimum is reached between the trough ($kx = 3\pi/2$) and the forward slope ($kx = \pi$).

To summarize, the variation of the vorticity with the wave phase is the result of the periodic stretching and tilting by wave orbital straining, as sketched in figure 18. Under the forward slope, the wave stretching weakens the streamwise vorticity and amplifies the vertical vorticity. Under the backward slope, the stretching incurs the opposite process. The tilting effect of the wave is the strongest under the wave crest and trough, while the tilting direction is opposite. As the wave passes, the periodic variation of the wave straining leads to fluctuations of vortices with the wave phase. To our knowledge, this is the first time that the vorticity dynamics in Langmuir turbulence is numerically analysed with wave-phase-resolved details. In the following section, we shall see that, by interacting with the local wave orbital

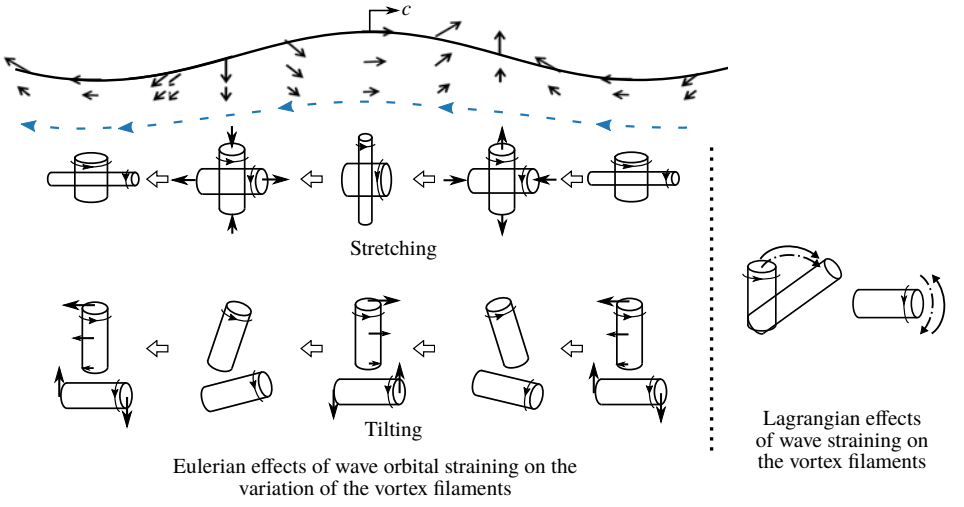

FIGURE 18. (Colour online) Sketch of the wave effect on the evolution of vortices. On the left part (discussed in § 5.4), the variation of the vortex filaments induced by the wave orbital straining is illustrated in the Eulerian frame. The upper row shows the stretching-induced vorticity fluctuations, and the lower row shows the tilting-induced vorticity fluctuations. Note that relative to the wave, the vortex is convected in the opposite direction of the wave propagation direction as indicated by the arrows along the dashed line. An extra quarter of wavelength is plotted for the purpose of illustrating the wave periodicity in space. On the right part (discussed in § 6), the Lagrangian cumulative effect of the wave on the vortex filaments is illustrated, where the solid and dash-dotted arrows denote the mean effect and the correlation effect, respectively.

straining, the wave-phase variation of the vorticity is an important factor contributing to the long-term vorticity evolution.

6. Perspective on cumulative effect of wave on vorticity evolution

Langmuir turbulence is attributed to the cumulative distortion imposed by the surface wave (Leibovich 1983; Thorpe 2004). In this section, the cumulative distortion effect of wave on wave-phase-averaged vorticity is analysed through Lagrangian average. First, in § 6.1, we assess the contributions from different effects, including the wave, current and turbulence, to the cumulative vorticity evolution. Then in § 6.2, the wave effect is decomposed based on the Lagrangian mean and fluctuation, where we find that the wave-phase variation of the vorticity is important to the cumulative vorticity evolution. The mechanism of how the wave-phase variation of the vorticity affects the long-term vorticity evolution is further discussed in § 6.3, which provides insights into the physical process of the wave distortion. At last, the relation between the CL vortex force and the modelling of the wave effect based on the Lagrangian decomposition is discussed in § 6.4.

Here, we continue focusing on ω_x and ω_z because the spanwise turbulence vorticity is relatively weak and is not directly affected by the wave (§ 5). The Lagrangian averaging (2.16) is applied to the vorticity evolution equations (5.2) and (5.3), and the equations governing the Lagrangian mean vorticity $\overline{\boldsymbol{\omega}}^L$ are

$$\frac{\overline{\mathrm{D}}^L\overline{\omega_x}^L}{\overline{\mathrm{D}}t} = \underbrace{\overline{\omega_x\frac{\partial u_c}{\partial x}}^L + \overline{\omega_z\frac{\partial u_c}{\partial z}}^L}_{\overline{\mathcal{D}_x^c}^L} + \underbrace{\overline{\omega_x\frac{\partial u_w}{\partial x}}^L + \overline{\omega_z\frac{\partial u_w}{\partial z}}^L}_{\overline{\mathcal{D}_x^w}^L} + \underbrace{\overline{\omega_x\frac{\partial u'}{\partial x} + \omega_y\frac{\partial u'}{\partial y} + \omega_z\frac{\partial u'}{\partial z}}^L}_{\overline{\mathcal{D}_x^t}^L}$$

$$\underbrace{\overline{-u'\frac{\partial \omega_x}{\partial x} - v'\frac{\partial \omega_x}{\partial y} - w'\frac{\partial \omega_x}{\partial z}}^L}_{\overline{\mathcal{T}_x^t}^L} + \underbrace{\overline{\nu\nabla^2\omega_x}^L - \overline{[\boldsymbol{\nabla}\times(\boldsymbol{\nabla}\cdot\boldsymbol{\tau})]_x}^L}_{\overline{\mathcal{F}_x}^L}; \tag{6.1}$$

$$\frac{\overline{\mathrm{D}}^L\overline{\omega_z}^L}{\overline{\mathrm{D}}t} = \underbrace{\overline{\omega_x\frac{\partial w_w}{\partial x}}^L + \overline{\omega_z\frac{\partial w_w}{\partial z}}^L}_{\overline{\mathcal{D}_z^w}^L} + \underbrace{\overline{\omega_x\frac{\partial w'}{\partial x} + \omega_y\frac{\partial w'}{\partial y} + \omega_z\frac{\partial w'}{\partial z}}^L}_{\overline{\mathcal{D}_z^t}^L}$$

$$\underbrace{\overline{-u'\frac{\partial \omega_z}{\partial x} - v'\frac{\partial \omega_z}{\partial y} - w'\frac{\partial \omega_z}{\partial z}}^L}_{\overline{\mathcal{T}_z^t}^L} + \underbrace{\overline{\nu\nabla^2\omega_z}^L - \overline{[\boldsymbol{\nabla}\times(\boldsymbol{\nabla}\cdot\boldsymbol{\tau})]_z}^L}_{\overline{\mathcal{F}_z}^L}. \tag{6.2}$$

The aforementioned sign-based average method is also applied here, i.e. the vorticity equations are multiplied by sign (ω_i) such that the positive and negative vorticities do not cancel each other during the averaging. The Lagrangian average gives the evolution of the Lagrangian mean vorticity $\overline{\omega_i}^L$ when the fluid elements are convected by the mean flow for several Lagrangian periods.

6.1. *Lagrangian vorticity dynamics*

The characteristics of the Lagrangian vorticity dynamics are found to depend mainly on La_t, and three representative cases, L1, L3 and S, are assessed. As pointed out above, the case L1 with $La_t = 0.35$ represents the Langmuir turbulence scenario where the wave forcing is strong, and the case L3 with $La_t = 0.9$ represents the condition when the wave forcing is relatively weak. The case S is the shear-driven turbulence without the wave. The three cases demonstrate the transition of vorticity balance from strong Langmuir turbulence to purely shear-driven turbulence.

We first look at the dynamics of the Lagrangian mean of the streamwise vorticity $\overline{\omega_x}^L$. As shown in figure 19(*a*), where the vertical profiles of the right-hand side terms in (6.1) are plotted, the positive contributions to $\overline{\omega_x}^L$ are mainly due to the distortion by the wave and current, $\overline{\mathcal{D}^w}^L$ and $\overline{\mathcal{D}^c}^L$, respectively. However, the vertical distributions of the two effects are different. The wave effect $\overline{\mathcal{D}^w}^L$ penetrates deeper into the domain and dominates in the region away from the surface. The distortion by the current, $\overline{\mathcal{D}^c}^L$, is small at most of the depths because of the weak current shearing associated with the strong vertical mixing in Langmuir turbulence (§ 3.1). Only when the viscous region at the surface is approached does the current effect become comparable to the wave effect. This indicates that the streamwise vorticity in most of the region is mainly enhanced by the wave straining.

As La_t increases and the current gradient becomes larger, the current effect becomes increasingly important in the generation of the streamwise vorticity. At $La_t = 0.5$ (case L2, results not plotted), the wave effect is still dominant at most of the depths. As La_t increases to 0.9 (case L3), the distortion by the current prevails over the wave effect, as shown in figure 19(*b*). In the shear-driven turbulence (case S), ω_x is completely driven by the tilting by the current (figure 19*c*).

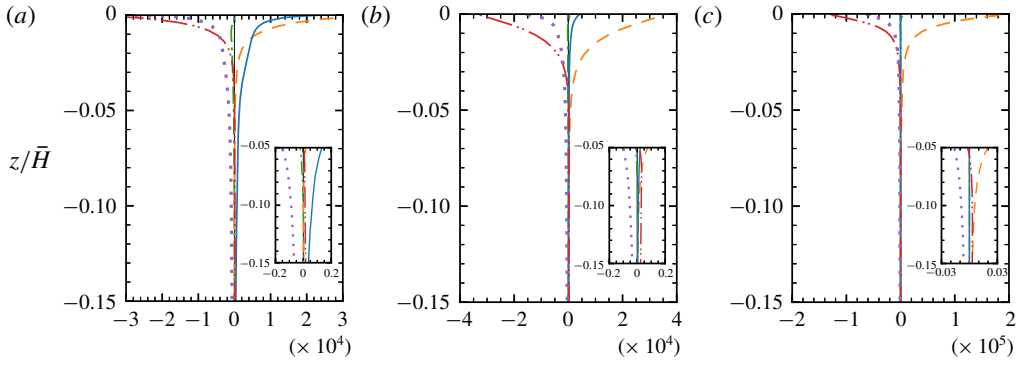

FIGURE 19. (Colour online) Vertical profiles of the terms in the Lagrangian-averaged vorticity equation for $\overline{\omega_x}^L$ (6.1) for (*a*) case L1, (*b*) case L3 and (*c*) case S: distortion by the wave $\overline{\mathcal{D}^w}^L$ (——), distortion by the current $\overline{\mathcal{D}^c}^L$ (– – –), distortion by the turbulence $\overline{\mathcal{D}^t}^L$ (— · · —), turbulence transport $\overline{\mathcal{T}^t}^L$ (— · —) and viscous force and SGS stress $\overline{\mathcal{F}}^L$ (· · · · · ·). The results are normalized by $u_*^2/\bar{H}^2$.

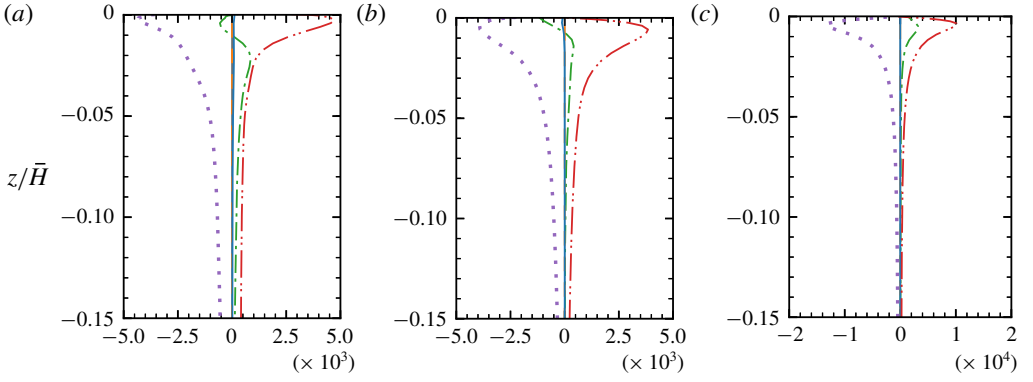

FIGURE 20. (Colour online) Vertical profiles of the terms in the Lagrangian-averaged vorticity equation for $\overline{\omega_z}^L$ (6.2) for (*a*) case L1, (*b*) case L3 and (*c*) case S: distortion by the wave $\overline{\mathcal{D}^w}^L$ (——), distortion by the turbulence $\overline{\mathcal{D}^t}^L$ (— · · —), turbulence transport $\overline{\mathcal{T}^t}^L$ (— · —) and viscous force and SGS stress $\overline{\mathcal{F}}^L$ (· · · · · ·). The results are normalized by $u_*^2/\bar{H}^2$.

The terms related to the dynamics of $\overline{\omega_z}^L$ (6.2) are plotted in figure 20. For the Langmuir turbulence cases L1 and L3 (figures 20*a* and 20*b*, respectively), the wave distortion effect, $\overline{\mathcal{D}^w}^L$, is negligible. This indicates that the wave straining barely has any cumulative effect on the vertical vorticity, in contrast to its enhancement effect on the streamwise vorticity. The current distortion effect, $\overline{\mathcal{D}^c}^L$, is not present in (6.2). However, the current can still generates vertical vorticity through $\omega_y \partial w'/\partial y$ in the turbulence distortion term $\overline{\mathcal{D}^t}^L$ because the current has a spanwise vorticity $\partial u_c/\partial z$. Vertical vorticity can be generated as the turbulence velocity gradient $\partial w'/\partial y$ turns the current-associated vorticity towards the vertical direction. Meanwhile, we note that $\partial w'/\partial y$ is associated with the streamwise vorticity. As a result, when the

shearing current amplifies the streamwise vorticity through $\overline{\mathcal{D}^c}^L$, the generation of the vertical vorticity is also enhanced. This process, associated with the current shearing, is consistent with the analyses by Kida & Tanaka (1994) and Teixeira & Belcher (2002, 2010), and is found to be strong in cases L3 and S where the current effect is dominant.

The above analyses of Lagrangian vorticity dynamics show that the wave distortion effect is the dominant factor in the generation of the vorticity in Langmuir turbulence. The wave cumulatively enhances the streamwise vorticity, but has a negligible net effect on the vertical vorticity. This behaviour is distinctively different from the vortex distortion by the current, which not only enhances the streamwise vorticity, but also induces an increase in the vertical vorticity (through the $\overline{\mathcal{D}^t}^L$ term as analysed above). Therefore, the wave leads to more effective amplification and elongation of the streamwise vortices, as observed in Langmuir turbulence.

6.2. *Lagrangian decomposition of wave effect*

To obtain a better understanding of how the wave straining enhances only the streamwise component of the vorticity but not the vertical component, we apply the Lagrangian-average-based decomposition defined in § 2.5,

$$\langle f\rangle = \overline{f}^L + f^l, \tag{6.3}$$

to the wave stretching and tilting terms $\overline{\mathcal{D}^w}^L$ in (6.1) and (6.2). To obtain the decomposition of $\overline{\mathcal{D}^w}^L$, we first invoke the triple decomposition, (2.12) and (2.13),

$$\overline{\mathcal{D}^w}^L = \overline{\boldsymbol{\omega}\cdot\boldsymbol{\nabla}\boldsymbol{u}_w}^L = \overline{(\langle\boldsymbol{\omega}\rangle + \boldsymbol{\omega}')\cdot\boldsymbol{\nabla}\boldsymbol{u}_w}^L. \tag{6.4}$$

Recalling that the wave velocity is obtained from the phase averaging, i.e. $\boldsymbol{\nabla}\boldsymbol{u}_w = \langle\boldsymbol{\nabla}\boldsymbol{u}_w\rangle$, we obtain

$$\overline{\mathcal{D}^w}^L = \overline{\langle\boldsymbol{\omega}\rangle\cdot\langle\boldsymbol{\nabla}\boldsymbol{u}_w\rangle}^L + \overline{\boldsymbol{\omega}'\cdot\langle\boldsymbol{\nabla}\boldsymbol{u}_w\rangle}^L. \tag{6.5}$$

Note that the Lagrangian average (2.16) is defined based on the phase averaging, therefore the second term on the right-hand side of (6.5) is zero. Then (6.5) can be further decomposed as

$$\overline{\mathcal{D}^w}^L = \overline{(\overline{\boldsymbol{\omega}}^L + \boldsymbol{\omega}^l)\cdot\left[\overline{\boldsymbol{\nabla}\boldsymbol{u}_w}^L + (\boldsymbol{\nabla}\boldsymbol{u}_w)^l\right]}^L = \overline{\boldsymbol{\omega}}^L\cdot\overline{\boldsymbol{\nabla}\boldsymbol{u}_w}^L + \overline{\boldsymbol{\omega}^l\cdot(\boldsymbol{\nabla}\boldsymbol{u}_w)^l}^L. \tag{6.6}$$

The Lagrangian-average-based decomposition of the each individual term in $\overline{\mathcal{D}^w}^L$ is

$$\overline{\omega_x\frac{\partial u_w}{\partial x}}^L = \overline{\omega_x}^L\overline{\frac{\partial u_w}{\partial x}}^L + \overline{\omega_x^l\left(\frac{\partial u_w}{\partial x}\right)^l}^L, \tag{6.7a}$$

$$\overline{\omega_z\frac{\partial u_w}{\partial z}}^L = \overline{\omega_z}^L\overline{\frac{\partial u_w}{\partial z}}^L + \overline{\omega_z^l\left(\frac{\partial u_w}{\partial z}\right)^l}^L, \tag{6.7b}$$

$$\overline{\omega_x\frac{\partial w_w}{\partial x}}^L = \overline{\omega_x}^L\overline{\frac{\partial w_w}{\partial x}}^L + \overline{\omega_x^l\left(\frac{\partial w_w}{\partial x}\right)^l}^L, \tag{6.7c}$$

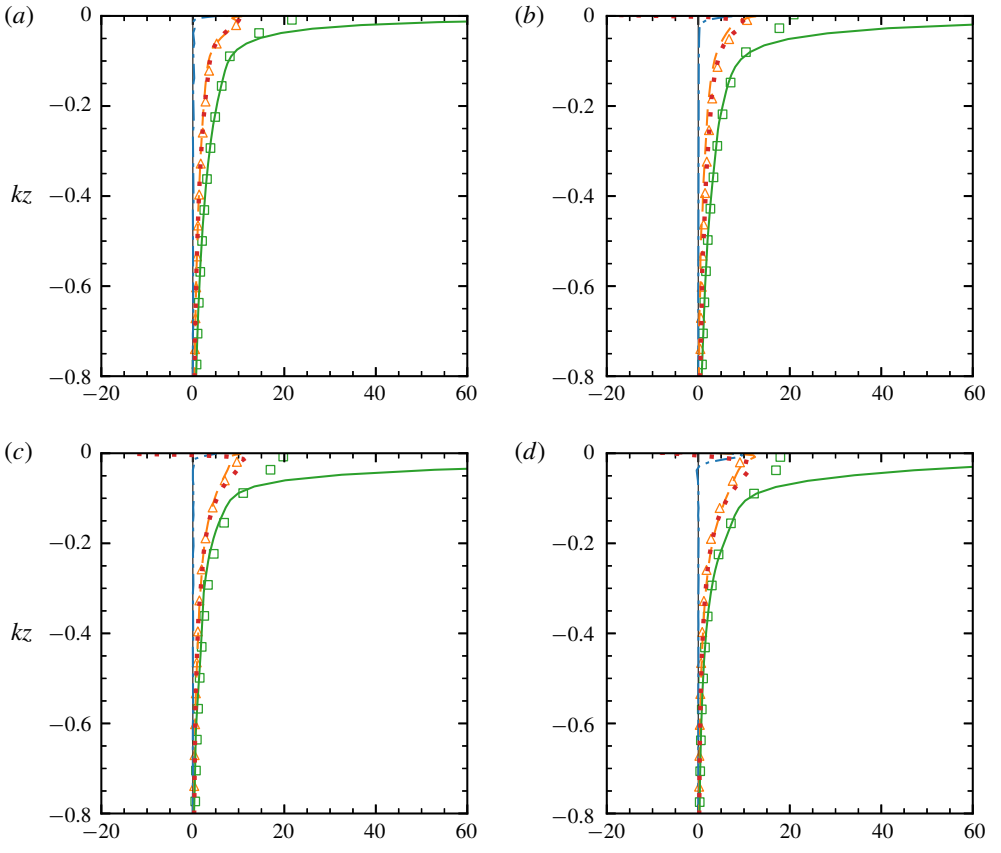

FIGURE 21. (Colour online) Lagrangian decomposition of the wave distortion effect $\overline{\mathcal{D}_x^w}^L$ (6.7*a*) and (6.7*b*) for (*a*) case L1, (*b*) case L1S, (*c*) case L2 and (*d*) case L3: mean effects $\overline{\omega_x}^L\overline{\partial u_w/\partial x}^L$ (— · —), $\overline{\omega_z}^L\overline{\partial u_w/\partial z}^L$ (——) and the estimation based on the potential wave solution (6.9) (□); correlation effects $\overline{\omega_x^l(\partial u_w/\partial x)^l}^L$ (– – –), $\overline{\omega_z^l(\partial u_w/\partial z)^l}^L$ (· · · · · ·) and the estimation based on (6.14*a*) or (6.14*b*) in § 6.3 (△). Note that (6.14*a*) and (6.14*b*) have the same values. The results are normalized by $u_* a^2 k^3 \omega$.

$$\overline{\omega_z \frac{\partial w_w}{\partial z}}^L = \underbrace{\overline{\omega_z}^L \overline{\frac{\partial w_w}{\partial z}}^L}_{\textit{mean effects}} + \underbrace{\overline{\omega_z^l \left(\frac{\partial w_w}{\partial z}\right)^l}^L}_{\textit{correlation effects}}. \tag{6.7d}$$

The first terms on the right-hand side of (6.7) are in the form of a product of two Lagrangian-averaged quantities, representing the effects of Lagrangian mean wave straining (§ 4.2) on the vorticity. In other words, these are the change rate of the vorticity if we neglect the wave-phase variation of the vorticity within the wave period. The second terms account for the contribution from the interactions between the wave-phase-varying vorticity and the local wave orbital straining. For brevity, we call the first terms the mean effects and the second terms the correlation effects.

The vertical profiles of the terms from the decomposition (6.7*a*) and (6.7*b*), which contribute to the cumulative evolution of streamwise vorticity (6.1), are plotted in

figure 21. The dominant terms are found to be

$$\overline{\omega_z}^L \overline{\frac{\partial u_w}{\partial z}}^L, \quad \overline{\omega_z^l \left(\frac{\partial u_w}{\partial z}\right)^l}^L, \quad \overline{\omega_x^l \left(\frac{\partial u_w}{\partial x}\right)^l}^L, \tag{6.8a–c}$$

which are all positive and hence enhance $\overline{\omega_x}^L$. The mean effect $\overline{\omega_z}^L \overline{\partial u_w/\partial z}^L$ represents the generation of the streamwise vorticity from the vertical vorticity component through the tilting by the Lagrangian wave shear gradient. The tilting effect increases towards the surface due to the stronger wave straining near the surface. When the surface is further approached, the tilting effect increases rapidly due to the strong $\overline{\partial u_w/\partial z}^L$ within the viscous surface boundary layer discussed in § 4.2. The variation of $\overline{\omega_z}^L \overline{\partial u_w/\partial z}^L$ is not fully shown in the vicinity of the surface in figure 21 because the viscous layer is thin and we focus mainly on the region below. Using the potential wave solution $\overline{\partial u_w/\partial z}^L = (ak)^2 \omega \mathrm{e}^{2kz}$ (Ardhuin & Jenkins 2006), we estimate the mean tilting effect as

$$\overline{\omega_z}^L \overline{\frac{\partial u_w}{\partial z}}^L \approx \overline{\omega_z}^L \mathrm{e}^{2kz} (ak)^2 \omega. \tag{6.9}$$

As shown in figure 21, this estimation agrees with the numerical solution below the surface layer, where the irrotational wave solution represents $\overline{\partial u_w/\partial z}^L$ well (figure 11). We also note here that the other mean effect, $\overline{\omega_x}^L \overline{\partial u_w/\partial x}^L$, is small because the Lagrangian mean stretching $\overline{\partial u_w/\partial x}^L$ is essentially zero (§ 4.2).

Other than the mean tilting effect, the two correlation terms, $\overline{\omega_z^l (\partial u_w/\partial z)^l}^L$ and $\overline{\omega_x^l (\partial u_w/\partial x)^l}^L$, also make appreciable contributions to the enhancement of $\overline{\omega_x}^L$. The contributions from the correlation terms indicate that the variation of the vorticity within a wave period is important to the long-term vorticity evolution. The quantification and the physical mechanism of the correlation effect are further discussed in § 6.3 below.

Next, we show the terms from (6.7*c*) and (6.7*d*) in figure 22, which contribute to the evolution of $\overline{\omega_z}^L$ (6.2). It is found that the dominant terms are

$$\overline{\omega_x}^L \overline{\frac{\partial w_w}{\partial x}}^L, \quad \overline{\omega_z^l \left(\frac{\partial w_w}{\partial z}\right)^l}^L, \quad \overline{\omega_x^l \left(\frac{\partial w_w}{\partial x}\right)^l}^L. \tag{6.10a–c}$$

The mean effect, $\overline{\omega_x}^L \overline{\partial w_w/\partial x}^L$, is positive, indicating that the Lagrangian wave shear gradient tends to tilt the streamwise vortices towards the vertical direction and increases the vertical vorticity. Note that the viscous surface layer does not affect $\overline{\partial w_w/\partial x}^L$ and thus does not lead to the sharp change of the profile near the surface. Also plotted in figure 22 is the estimation of the mean effect using the potential wave solution $\overline{\partial w_w/\partial x}^L = (ak)^2 \omega \mathrm{e}^{2kz}$,

$$\overline{\omega_x}^L \overline{\frac{\partial w_w}{\partial x}}^L \approx \overline{\omega_x}^L \mathrm{e}^{2kz} (ak)^2 \omega, \tag{6.11}$$

which yields a good agreement with the simulation result. On the other hand, the correlation effects, $\overline{\omega_z^l (\partial w_w/\partial z)^l}^L$ and $\overline{\omega_x^l (\partial w_w/\partial x)^l}^L$, are negative, which, interestingly,

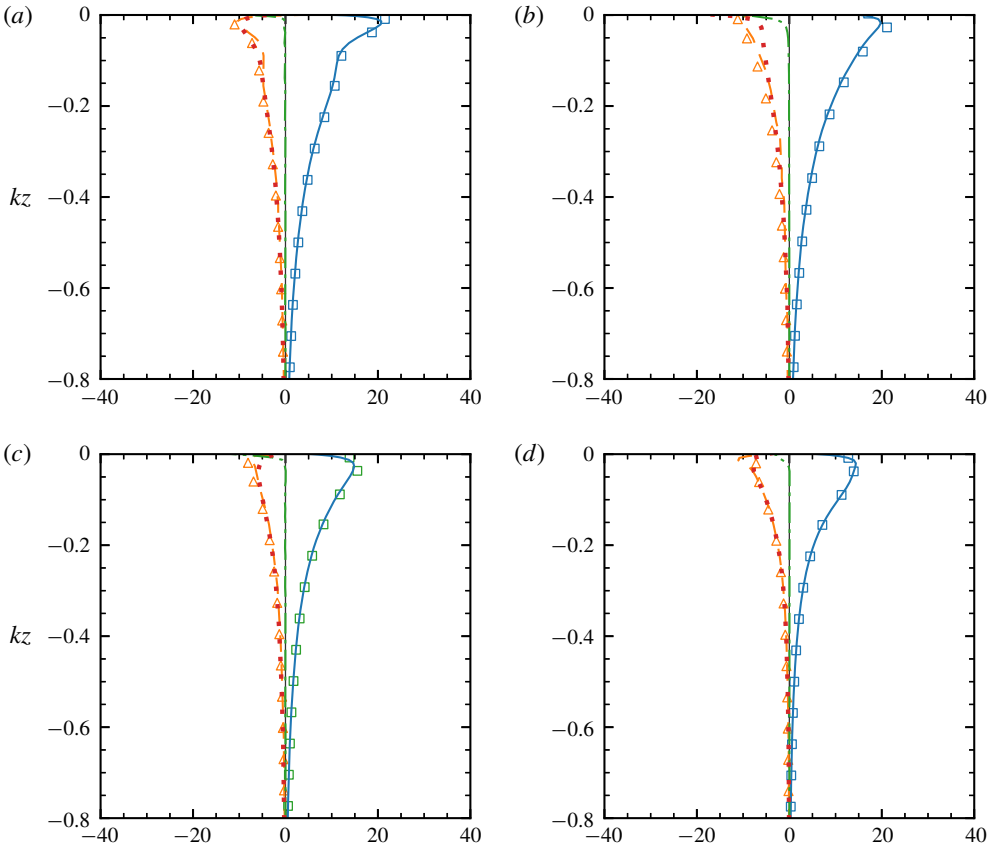

FIGURE 22. (Colour online) Lagrangian decomposition of the wave distortion effect $\overline{\mathcal{D}_z^w}^L$ (6.7*c*) and (6.7*d*) for (*a*) case L1, (*b*) case L1S, (*c*) case L2 and (*d*) case L3: mean effects $\overline{\omega_x}^L\overline{\partial w_w/\partial x}^L$ (——), $\overline{\omega_z}^L\overline{\partial w_w/\partial z}^L$ (— · —) and the estimation based on the potential wave solution (6.11) (□); correlation effects $\overline{\omega_x^l(\partial w_w/\partial x)^l}^L$ (– – –), $\overline{\omega_z^l(\partial w_w/\partial z)^l}^L$ (· · · · · ·) and the estimation based on (6.15*a*) or (6.15*b*) in § 6.3 (△). Note that (6.15*a*) or (6.15*b*) have the same values. The results are normalized by $u_*a^2k^3\omega$.

cancel the mean effect. The cancellation between the mean effect and the correlation effect results in nearly no net change of $\overline{\omega_z}^L$, in direct contrast to $\overline{\omega_x}^L$ discussed in § 6.1.

In summary, the correlation effect associated with the wave-phase variation of the vorticity is found to play an important role in the cumulative wave distortion of vortices. Notably, the near-zero change of the vertical vorticity is a result of the cancellation between the mean tilting effect and the correlation effect. Meanwhile, the correlation effect is as important as the mean effect in enhancing the streamwise vorticity. The mean effect and the correlation effect on the Lagrangian vorticity evolution are illustrated in the right part of figure 18.

6.3. *Quantification of correlation effect in cumulative vorticity dynamics*

Due to the importance of the correlation effect shown in § 6.2, we further investigate it by quantifying the correlation terms to understand the underlying process. Because

the correlation effect involves the interactions between the Lagrangian fluctuation of the vorticity and the wave straining, we first estimate the fluctuation of the vorticity, $\boldsymbol{\omega}^l$, and then consider its correlation with the wave straining, $(\boldsymbol{\nabla u}_w)^l$. Based on the definitions in (2.16) and (2.18), the Lagrangian fluctuation is essentially the variation with the wave phase, which is shown in § 5.4 to be mainly driven by the wave orbital straining. Therefore, the evolution of $\boldsymbol{\omega}^l$ is estimated by

$$\frac{D\boldsymbol{\omega}^l}{Dt} \approx \overline{\boldsymbol{\omega}}^L \cdot (\boldsymbol{\nabla u}_w)^l, \tag{6.12}$$

and the vorticity fluctuation with the wave phase is then

$$\omega_x^l \approx \overline{\boldsymbol{\omega}}^L \cdot \int (\boldsymbol{\nabla} u_w)^l \,\mathrm{d}t, \quad \omega_z^l \approx \overline{\boldsymbol{\omega}}^L \cdot \int (\boldsymbol{\nabla} w_w)^l \,\mathrm{d}t. \tag{6.13a,b}$$

Using (6.13), we can calculate the leading order of the correlation terms in (6.7). The details of the derivations are given in appendix D.

As derived in appendix D (D 4 and D 5), the correlation terms from (6.7*a*) and (6.7*b*), which affect the evolution of $\overline{\omega_x}^L$ (6.1), are

$$\overline{\omega_x^l \left(\frac{\partial u_w}{\partial x}\right)^l}^L \approx \overline{\left[\overline{\omega_z}^L \int \left(\frac{\partial u_w}{\partial z}\right)^l \mathrm{d}t\right] \left(\frac{\partial u_w}{\partial x}\right)^l}^L \approx 0.5\,\overline{\omega_z}^L \mathrm{e}^{2kz}(ak)^2\omega, \tag{6.14a}$$

$$\overline{\omega_z^l \left(\frac{\partial u_w}{\partial z}\right)^l}^L \approx \overline{\left[\overline{\omega_z}^L \int \left(\frac{\partial w_w}{\partial z}\right)^l \mathrm{d}t\right] \left(\frac{\partial u_w}{\partial z}\right)^l}^L \approx 0.5\,\overline{\omega_z}^L \mathrm{e}^{2kz}(ak)^2\omega. \tag{6.14b}$$

The estimations at the end of (6.14*a*) and (6.14*b*) are plotted in figure 21 and agree with the simulation result. The combined contribution from the two correlation terms is approximately the same as the mean effect (6.9). We also note that the magnitudes of the above correlation terms are positively proportional to $\overline{\omega_z}^L$, which means that the streamwise vorticity of the same sign as $\overline{\omega_z}^L$ is generated from the correlation effect as if the vertical vortices are 'tilted' towards the streamwise direction. The physical processes associated with (6.14*a*) and (6.14*b*) are illustrated in figures 23(*a*) and 23(*b*), respectively, and discussed in more detail below.

The interaction between $\overline{\omega_z}^L \int (\partial u_w/\partial z)^l \,\mathrm{d}t$ and $(\partial u_w/\partial x)^l$ in (6.14*a*) is illustrated in figure 23(*a*). In (6.14*a*), $\overline{\omega_z}^L \int (\partial u_w/\partial z)^l \,\mathrm{d}t$ represents the periodic tilting of vertical vortex filaments, which induces streamwise vorticity fluctuation ω_x^l, as shown in the left part of figure 18 and the first row of figure 23(*a*). The vorticity fluctuation ω_x^l is positively correlated with the wave orbital straining $(\partial u_w/\partial x)^l$, leading to a net increase in the streamwise vorticity. For example, if $\overline{\omega_z}^L$ is positive, the tilting results in positive ω_x^l under the backward slope and negative ω_x^l under the forward slope. The positive ω_x^l is amplified under the backward slope due to the streamwise stretching, which outweighs the negative ω_x^l that is suppressed under the forward slope due to compression (figure 23*a*). As a result, net positive streamwise vorticity is generated. A similar process occurs with negative $\overline{\omega_z}^L$, which eventually generates negative streamwise vorticity (not plotted in figure 23*a*). In summary, the correlation effect (6.14*a*) amplifies the streamwise vorticity, due to the periodic tilting of vertical vortex filaments combined with streamwise stretching and compression.

Figure 23(*b*) illustrates the correlation between $\overline{\omega_z}^L \int (\partial w_w/\partial z)^l \,\mathrm{d}t$ and $(\partial u_w/\partial z)^l$ in (6.14*b*). The value of $\overline{\omega_z}^L \int (\partial w_w/\partial z)^l \,\mathrm{d}t$ represents the fluctuation ω_z^l induced

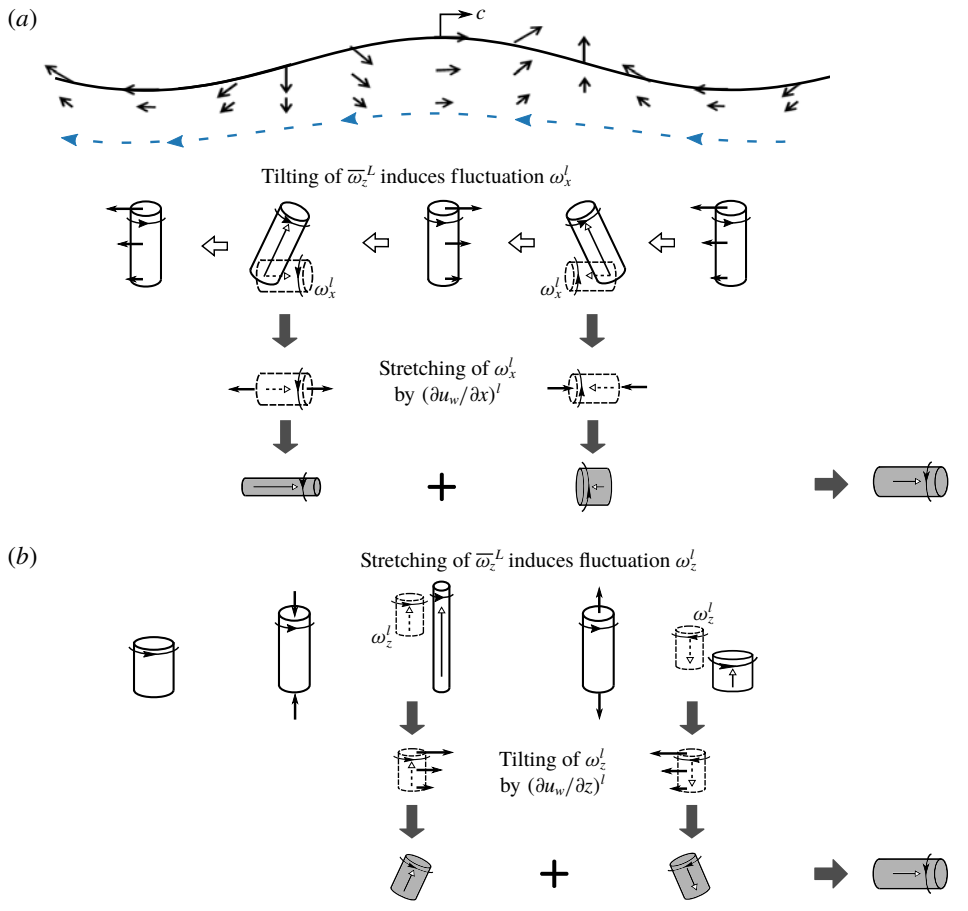

FIGURE 23. Sketch of the correlation between the fluctuating vorticity and the wave straining, and how the correlation contributes to the cumulative evolution of $\overline{\omega_x}^L$: (*a*) the correlation between ω_x^l and $(\partial u_w/\partial x)^l$ (6.14*a*); (*b*) the correlation between ω_z^l and $(\partial u_w/\partial z)^l$ (6.14*b*). The first rows of (*a*) and (*b*), which are similar to the left part of figure 18, show the generation of the Lagrangian fluctuation, $\boldsymbol{\omega}^l$ (vortex tubes with dashed lines), due to the tilting and stretching of vertical vortices, respectively. The second rows of (*a*) and (*b*) illustrate the interaction of $\boldsymbol{\omega}^l$ with the local wave straining of stretching and tilting, respectively. The third rows illustrate the net vorticity generated by the correlation effect, denoted by solid grey tubes.

by the vertical stretching and compression of vertical vortex filaments (the left part of figure 18 and the first row of figure 23*b*). If $\overline{\omega_z}^L$ is positive, the resulting ω_z^l is positive under the crest and negative under the trough. Because $(\partial u_w/\partial z)^l$ is positive under the crest, the vorticity vector with positive ω_z^l is tilted clockwise and generates positive streamwise vorticity. Under the trough, $(\partial u_w/\partial z)^l$ is negative and the counter-clockwise tilting of the vorticity vector with negative ω_z^l also generates positive streamwise vorticity. Therefore, positive streamwise vorticity is cumulatively generated. The correlation process for negative $\overline{\omega_z}^L$ is similar, and the net effect is the increase of negative streamwise vorticity. The above discussion explains (6.14*b*).

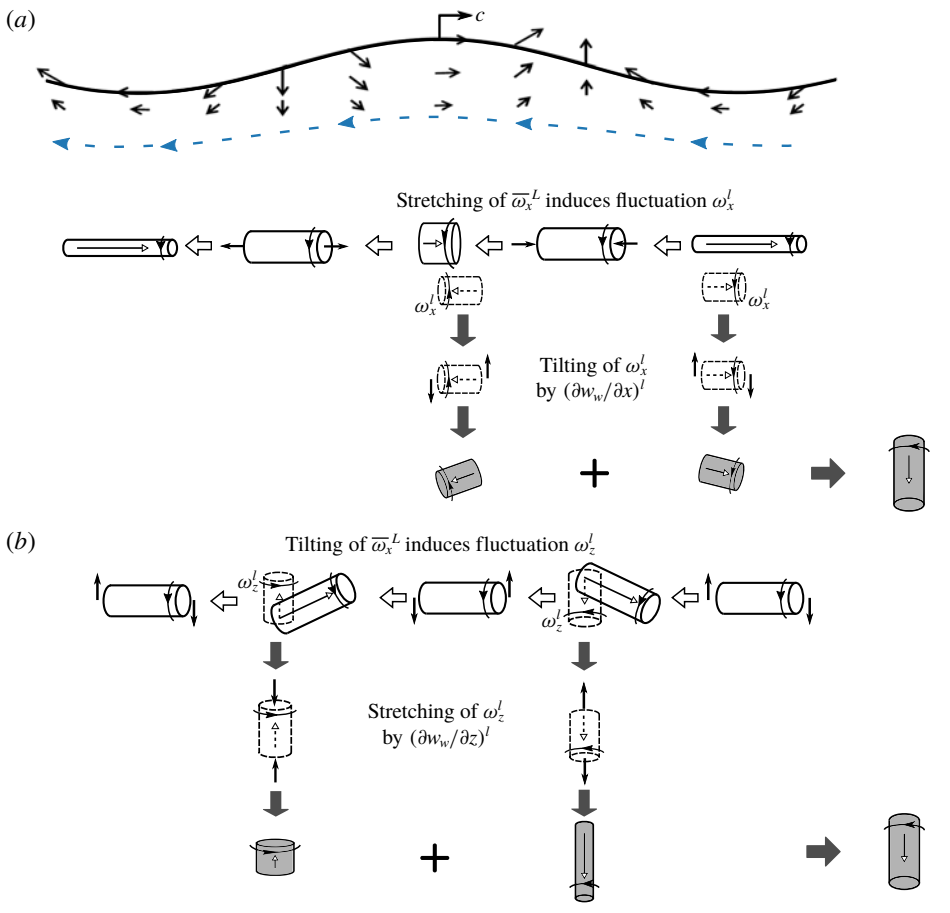

FIGURE 24. (Colour online) Sketch of the correlation between the fluctuating vorticity and the wave straining, and how the correlation contributes to the cumulative evolution of $\overline{\omega_z}^L$: (*a*) the correlation between ω_x^l and $(\partial w_w/\partial x)^l$ (6.15*a*); (*b*) the correlation between ω_z^l and $(\partial w_w/\partial z)^l$ (6.15*b*). The first rows of (*a*) and (*b*), which are similar to the left part of figure 18, show the generation of the Lagrangian fluctuation, $\boldsymbol{\omega}^l$ (vortex tubes with dashed lines), due to the stretching and tilting of streamwise vortices, respectively. The second rows of (*a*) and (*b*) illustrate the interaction of $\boldsymbol{\omega}^l$ with the local wave straining of tilting and stretching, respectively. The third rows illustrate the net vorticity generated by the correlation effect, denoted by solid grey tubes.

Next, we discuss the correlation terms in (6.7*c*) and (6.7*d*) for the dynamics of $\overline{\omega_z}^L$ (6.2). Following appendix D (D 6 and D 7), we have

$$\overline{\omega_x^l\left(\frac{\partial w_w}{\partial x}\right)^l}^L \approx \overline{\left[\overline{\omega_x}^L\int\left(\frac{\partial u_w}{\partial x}\right)^l \mathrm{d}t\right]\left(\frac{\partial w_w}{\partial x}\right)^l}^L \approx -0.5\,\overline{\omega_x}^L \mathrm{e}^{2kz}(ak)^2\omega, \quad (6.15a)$$

$$\overline{\omega_z^l\left(\frac{\partial w_w}{\partial z}\right)^l}^L \approx \overline{\left[\overline{\omega_x}^L\int\left(\frac{\partial w_w}{\partial x}\right)^l \mathrm{d}t\right]\left(\frac{\partial w_w}{\partial z}\right)^l}^L \approx -0.5\,\overline{\omega_x}^L \mathrm{e}^{2kz}(ak)^2\omega. \quad (6.15b)$$

As shown in figure 22, the estimation given by (6.15*a*) and (6.15*b*) is also in good agreement with the LES result. Note that the two correlation terms are related to $\overline{\omega_x}^L$, and they together cancel the mean tilting effect (6.11), indicating that the correlation effect effectively prevents the streamwise vortices from being tilted back to the vertical direction, consistent with preceding analyses of the Lagrangian vorticity dynamics. Figure 24 illustrates the correlations between the vorticity fluctuation and the wave straining associated with (6.15*a*) and (6.15*b*).

Equation (6.15*a*) reduces to the interaction between the vorticity fluctuation $\overline{\omega_x}^L \int (\partial u_w/\partial x)^l$ and the local wave straining $(\partial w_w/\partial x)^l$, which is sketched in figure 24(*a*). The vorticity fluctuation is associated with the periodic stretching and compression of $\overline{\omega_x}^L$ by the wave, as illustrated in the left part of figure 18 and the first row of figure 24(*a*). If $\overline{\omega_x}^L$ is positive, the corresponding ω_x^l is positive under the trough and negative under the crest. Under the trough, the negative $(\partial w_w/\partial x)^l$ tilts the positive vorticity vector ω_x^l clockwise and results in the generation of negative vertical vorticity. Under the crest, both $(\partial w_w/\partial x)^l$ and ω_x^l reverse signs, which still leads to negative vertical vorticity. As a result, net negative vertical vorticity is generated. For negative $\overline{\omega_x}^L$, the above correlation process results in net positive vertical vorticity. The above discussion explains (6.15*a*).

The correlation between $\overline{\omega_x}^L \int (\partial w_w/\partial x)^l \,\mathrm{d}t$ and $(\partial w_w/\partial z)^l$ in (6.15*b*) is illustrated in figure 24(*b*). The value of $\overline{\omega_x}^L \int (\partial w_w/\partial x)^l \,\mathrm{d}t$ represents the vertical vorticity fluctuation ω_z^l generated from the tilting of streamwise vortex filaments (the left part of figure 18 and the first row of figure 24*b*). If $\overline{\omega_x}^L$ is positive, the tilting leads to negative ω_z^l under the forward slope and positive ω_z^l under the backward slope. The negative ω_z^l is amplified by the vertical stretching due to the positive $(\partial w_w/\partial z)^l$ under the forward slope. On the other hand, under the backward slope, the positive ω_z^l is suppressed by the compression due to the negative $(\partial w_w/\partial z)^l$. Therefore, the negative ω_z^l outweighs the positive ω_z^l, and net negative vertical vorticity is generated. The correlation process for negative $\overline{\omega_x}^L$ is similar, which results in net positive vertical vorticity. The above discussion explains (6.15*b*).

To summarize, the correlation effects in (6.14*a*) and (6.14*b*) indicate that streamwise vorticity can be generated from the interactions between the wave straining and the vorticity fluctuation induced by the periodic tilting and stretching of vertical vortices. This means that the mean effect and the correlation effect together 'tilt' vertical vortices towards the streamwise direction, as illustrated step by step in figure 23 and summarized in the right part of figure 18. Furthermore, the streamwise vorticity generated by the correlation effect has the same estimated value as that generated by the mean tilting effect (6.9). On the other hand, (6.15*a*) and (6.15*b*) represent the generation of vertical vorticity from the correlation between the wave straining and the vorticity fluctuation due to the stretching and tilting of streamwise vortices (figure 24). This correlation effect, of which the values are opposite to the mean tilting effect (6.11), effectively cancels the tilting of the streamwise vortex filaments by the mean effect (the right part of figure 18). The physical processes underlying the correlation effects indicate that the phase variation of the vorticity within a wave period is important to the cumulative vorticity evolution in Langmuir turbulence.

6.4. *Discussion on the CL vortex force*

Now we compare the above analyses of the cumulative vorticity dynamics with the vortex force in the CL vorticity equation (Craik & Leibovich 1976)

$$\boldsymbol{\nabla} \times (\boldsymbol{u}_s \times \boldsymbol{\omega}) = -\boldsymbol{u}_s \cdot \boldsymbol{\nabla}\boldsymbol{\omega} + \boldsymbol{\omega} \cdot \boldsymbol{\nabla}\boldsymbol{u}_s. \tag{6.16}$$

Here, $\boldsymbol{u}_s \cdot \nabla \boldsymbol{\omega}$ is the convection of the vorticity due to the wave Stokes drift, and $\boldsymbol{\omega} \cdot \nabla \boldsymbol{u}_s$ represents the change rate of the vorticity due to vortex distortion by the wave Stokes drift. For uni-directional waves in the streamwise direction, the Stokes drift only has one non-zero component that varies in the vertical direction, i.e. $\boldsymbol{u}_s = (u_s(z), 0, 0)$. The vortex distortion $\boldsymbol{\omega} \cdot \nabla \boldsymbol{u}_s$ reduces to

$$\boldsymbol{\omega} \cdot \nabla \boldsymbol{u}_s|_x = \omega_z \frac{\partial u_s}{\partial z}, \quad \boldsymbol{\omega} \cdot \nabla \boldsymbol{u}_s|_y = \boldsymbol{\omega} \cdot \nabla \boldsymbol{u}_s|_z = 0. \tag{6.17a,b}$$

The only vorticity distortion term, $\omega_z(\partial u_s/\partial z)$, appears in the x-direction. It indicates that the vertically varying Stokes drift acts like a shearing effect that tilts vertical vorticity filaments to generate streamwise vorticity.

If we use $u_s = a^2 k\omega \mathrm{e}^{2kz}$ (Phillips 1977), the generation rate of streamwise vorticity due to the Stokes drift is

$$\omega_z \frac{\partial u_s}{\partial z} = 2\omega_z \mathrm{e}^{2kz}(ak)^2\omega. \tag{6.18}$$

Compared with our analyses of the Lagrangian dynamics of the vorticity (§ 6.2 and 6.3), (6.18) is consistent with the combined contribution from the mean effect (6.9) and the correlation effect (6.14). On the other hand, the vortex force has no effect on the vertical vorticity, which is also consistent with our Lagrangian analysis above that the correlation effect (6.15) cancels the mean effect (6.11) in the evolution of vertical vorticity. Therefore, the vortex force modelling of the wave effect on the wave-phase-averaged vorticity agrees with our wave-phase-resolved simulation and analyses.

The agreement is interesting yet not surprising. In the derivation of the CL equations (Craik & Leibovich 1976; Leibovich 1977*b*), the estimation of the order of magnitude and the multiscale asymptotic analysis show that the first-order perturbation to the vorticity is driven by the interactions between the wave and the leading-order (averaged) vorticity; then the first-order vorticity perturbation interacts with the wave cumulatively, of which the effect is obtained through an integration, leading to the vortex force term. The first-order vorticity perturbation estimated in the CL theory is similar to the phase variation of the vorticity in our Lagrangian analysis in that they both are related to the wave orbital straining and the mean vorticity (§ 5.4 and the quantitative estimation 6.13*a*,*b*). In other words, the vortex force includes the effect of the wave-phase-correlated vorticity fluctuation and models it using the wave-phase-averaged quantities, therefore the vortex force shows good agreement with our evaluation of the wave effect. This again confirms that the fluctuating vorticity is important to the correct modelling of the wave-phase-averaged vorticity dynamics.

The Lagrangian decomposition of the wave distortion terms separates the effect of the wave-phase-correlated fluctuating vorticity from the mean effect, further revealing the physical process underlying the phase-averaged vorticity dynamics. The increase of the streamwise vorticity, which appears to be due to the tilting of the vertical vortices by the Stokes drift according to the Stokes force, is caused by two effects, the mean tilting by the Lagrangian wave shear gradient and the 'oscillatory tilting' due to the correlation between the vorticity fluctuation and the wave orbital straining within a wave period. The mean effect (6.9) and the correlation effect (6.14) both account for half of the total increase rate of the streamwise vorticity. By contrast, for the vertical vorticity, the mean effect (6.11) and the correlation effect (6.15) cancel each other, which is why while the wave distortion turns vertical vortices into horizontal

vortices, it does not turn the latter back to the former. Therefore, the phase variation of the vorticity and its associated correlation effect is as crucial as the effect of the Lagrangian wave velocity gradient.

It should be pointed out that both the CL modelling and the present study focus on the first-order moments of turbulence statistics, i.e. the wave-phase-averaged vorticity (or equivalently velocity after integration). High-order moments, such as the Reynolds stress and turbulent kinetic energy (TKE), are also important to various applications but are more complex to model because they are often associated with stronger nonlinear effects. Zhou (1999) conjectured that the nonlinear interactions between the wave straining and the turbulence fluctuations with time scales similar to the wave period lead to the differences in Reynolds stress between the wave-phase-resolved simulation and the CL-based simulation. Meanwhile, it is evident from the analyses of the correlation effects in the vorticity dynamics that the wave-phase-correlated turbulence vorticity contributes to the wave-phase-averaged vorticity through its correlation with the wave straining, which we show can be modelled using the phase-averaged vorticity as (6.14) and (6.15). For high-order moments, it is not clear yet whether such correlation effects can be accounted for by the wave-phase-averaged equations. For example, in wall turbulence, the nonlinear interaction among vortices is an important mechanism for the generation of Reynolds stress (Ganapathisubramani, Longmire & Marusic 2003). The wave-phase-correlated fluctuating vortices may also have effects on the wave-phase-averaged Reynolds stress through nonlinearity. The effects of the wave-phase-correlated turbulence fluctuations on higher-order moments of turbulence statistics, which are beyond the scope of this paper, should be investigated in future studies.

7. Conclusions

The purpose of this study is to mechanistically investigate the wave effects on turbulence vorticity in Langmuir turbulence using wave-phase-resolved simulation. The unified simulation of the surface wave and turbulence fields is enabled by the wave-phase-resolved LES on a surface-fitted curvilinear grid. This approach resolves the wave effect explicitly, and thus avoids the modelling of the wave effects as in the CL-based simulations in the literature. In this work, we set up LES of the turbulent flow with wind shear stress applied at the wave surface subject to fully nonlinear free-surface kinematic and dynamic boundary conditions. This numerical set-up facilitates mechanistic analyses of the role of wave in the vorticity evolution. We have been able to gain insights into the direct distortion of turbulence vorticity by the wave orbital straining, and the long-term effects of the wave straining on the wave-phase-averaged vorticity.

To analyse the current, wave and turbulence in the wave-phase-resolved frame, we have proposed a triple decomposition method based on the GLM theory to separate the wave-induced velocity and the current. After examining the current profile, the surface flow structures and the vortex structures, we have found that the wave-phase-resolved simulation successfully captures the characteristic features of Langmuir turbulence. The current is nearly uniformly distributed over the water column due to the enhanced vertical mixing associated with the Langmuir turbulence. The windrows are illustrated by tracer particles. Both the instantaneous vorticity field and the reconstructed vortex structure using the LSE method show that quasi-streamwise vortices dominate the near-surface region. Compared with the vortices in a shear-driven flow, the vortices in Langmuir turbulence are more elongated in the streamwise direction and usually

appear in pairs. Most interestingly, we have observed a strong dependence of the distribution of the vortices with the wave phase.

To understand the wave effect on the turbulence vorticity, the wave properties are assessed, including the orbital straining varying with the wave phase and the Lagrangian mean wave straining (figure 12). The analyses of the wave orbital straining and the Lagrangian straining show that the wave is largely irrotational. The viscosity and the imposed surface shear stress only affect the wave motion in a thin viscous surface layer.

We then investigated the variation of the vortex structures and the vorticity statistics with the wave phase. Both the length and tilting angles of the vortices are found to be dependent on the wave phase. The enstrophy and the histograms of the inclination angles of the vorticity vectors also show variation with the wave phase. The analyses of the vorticity evolution equations reveal that the wave-phase variation of the vorticity and the resulting vortex structure are caused by the periodic stretching and tilting of the wave straining (figure 18). The streamwise vortices are stretched by the wave normal straining under the backward slope and compressed under the forward slope. The vertical vortices are stretched under the forward slope and compressed under the backward slope. Under the wave crest, the wave shear straining turns streamwise vortices and vertical vortices in the counter-clockwise and clockwise directions, respectively. Under the wave trough, the tilting directions reverse.

Besides the direct distortion effects of the wave on the phase variation of vorticity statistics, we have also analysed the vorticity dynamics in the Lagrangian frame to study the cumulative effects of the wave straining. In Langmuir turbulence, the wave straining leads to a cumulative enhancement of the streamwise vorticity, while its net effect on the vertical vorticity is negligible. This results in an overwhelming titling of vortices to the streamwise direction, and the elongation of the vortices.

To understand the mechanisms of the wave distortion effect, we have employed a Lagrangian-based Reynolds decomposition to analyse the effects of the Lagrangian mean quantities and the effects of the correlation between the wave-phase-dependent fluctuations. It is found that the phase correlation between the vorticity fluctuations and the wave orbital straining results in a net contribution to the streamwise vorticity, working together with the Lagrangian mean straining to tilt vertical vortices to the streamwise direction. On the other hand, the correlation effect cancels the tendency of the mean effect to increase the vertical vorticity, resulting in a negligible net change in the vertical vorticity. Therefore, the wave-phase variation of the turbulence vorticity is an important factor for the wave distortion effects to be selective on the different vorticity components. Overall, the stretching and tilting of the vorticity by the wave straining results in the enhancement of the streamwise vorticity. Because the streamwise vortical structures are important to the generation of Reynolds shear stress (McWilliams *et al.* 1997; Teixeira & Belcher 2002; Ganapathisubramani *et al.* 2003), the dominance of the streamwise vortices leads to a more efficient vertical mixing in the ocean surface boundary layer.

We have also performed a quantitative analysis of the correlation effect of the wave-phase-dependent fluctuations and obtained a physical picture of how the correlation effect contributes to the cumulative vorticity evolution. For the increase of the streamwise vorticity, the correlation effect is related to the vorticity variation induced by the vertical vorticity (figure 23). On the other hand, the correlation terms in the evolution of the vertical vorticity are related to the vorticity variation induced by the streamwise vorticity (figure 24). The vortex force modelling of the wave-phase-averaged vorticity has been found to agree with our quantitative

analyses of the combined mean and correlation effects in the cumulative vorticity dynamics because the effect of the fluctuating vorticity is modelled using the wave-phase-averaged quantities in the multiscale asymptotic analysis.

The present study is performed at a moderate Reynolds number $Re_\tau = 2000$, which is lower than the realistic oceanic environment (§ 2.4). In appendix E, a simulation of Langmuir turbulence with $Re_\tau = 500$ is performed and shows that the vorticity distortion terms associated with the wave straining are qualitatively the same as those from $Re_\tau = 2000$. The result suggests that the fundamental mechanism of the wave effect on the turbulence vorticity is insensitive to the Reynolds number and we conjecture that the mechanism can apply to higher Reynolds number flows. This is likely similar to the fact that the features of the turbulence structures near the boundary are weakly dependent on the Reynolds number in other types of flows (Klewicki *et al.* 1995; Morris *et al.* 2007).

We shall also note that under realistic conditions, misaligned wind and wave can occur due to swells and non-equilibrium wind seas (Gnanadesikan & Weller 1995; Polonichko 1997; Van Roekel *et al.* 2012; Sullivan *et al.* 2012; McWilliams *et al.* 2013; Rabe *et al.* 2014; Chen *et al.* 2016). Compared with the canonical condition considered in this study where the wind and the wave are co-aligned, the orientation of Langmuir cells is found to depend on the angles between the wave and wind. In terms of the vorticity dynamics, the tilting and stretching direction of the vorticity by the surface wave is not the same as the tilting direction of the wind-shear-driven current. The two mechanisms compete with each other and affect the balance of the vorticity evolution equations (6.1) and (6.2). In some cases, the current and wave may apply opposing effect on the vorticity distortion and suppress the Langmuir turbulence. However, for the wave straining effect on the vorticity considered in this work, $\overline{\boldsymbol{\omega}\cdot\boldsymbol{\nabla}\boldsymbol{u}_w}^L$, because the order of magnitude of $\boldsymbol{u}_w$ is significantly larger than the turbulence velocity scale, we conjecture that the modelling of the mean effect and the fluctuation effect can be generalized to apply to the misaligned cases. This can be evaluated in future work using the wave-phase-resolved simulations.

The vorticity and coherent vortical structures are important features of turbulent flows. The analyses of vorticity tilting and stretching due to the mean and correlation effects provide better understanding of the dynamical connection between the wave distortion and the generation of the turbulence vorticity in Langmuir turbulence. The new perspective highlights the role of the wave-phase-coherent turbulence in the dynamics of wave–turbulence interactions, i.e. the correlation effects. These findings also suggest considering the potential importance of the wave-phase-coherent turbulent motions in other aspects of the wave–turbulence interactions. For example, the CL equation and the Lagrangian mean vorticity evolution both describe the wave-phase-averaged quantities of the flow that are first-order moments of turbulence statistics (e.g. velocity or vorticity). Considering that the vortices are closely associated with the generation of the Reynolds shear stress and the production of the TKE, the fluctuating vortices due to the stretching and tilting also indicate the variation of the Reynolds stress and TKE with the wave phase (Xuan & Shen 2019), and the present work provides a possibility to investigate and quantify other wave-phase-correlated turbulence statistics. In future work, it would be desirable to investigate the effects of the wave-phase-dependent turbulent motions on higher-order turbulence statistics, such as the TKE and Reynolds stresses, and their relations with the wave-phase-averaged turbulence statistics.

Acknowledgements

This work is supported by the Office of Naval Research, National Science Foundation and Minnesota Sea Grant.

Appendix A. Surface pressure for maintaining the wave amplitude

Assuming that the elevation of the surface wave is $\eta(x, t) = a_t(t) \sin \varphi(x, t)$, where the wave amplitude a_t and the phase φ are evaluated at every time step, the pressure p_a is given by

$$p_a = p_0 \cos \varphi, \tag{A 1}$$

which lags the wave by a phase difference of $\pi/2$. The energy input rate over one wavelength from the applied pressure is

$$\frac{\mathrm{d}E}{\mathrm{d}t} = -\int_0^{\lambda} \eta_t p_a \,\mathrm{d}x = \frac{a\omega p_0}{2}\lambda. \tag{A 2}$$

Because the energy difference from the target wave amplitude is $\Delta E = \rho g(a^2 - a_t^2)\lambda/2$, where a is the target wave amplitude, we specify p_0 as

$$p_0 = \frac{\Delta E}{\Delta t}\frac{2}{a\omega\lambda} = \frac{\rho(a^2 - a_t^2)c}{a\Delta T} \tag{A 3}$$

to supply energy to maintain the wave amplitude or suppress the wave. Here, ΔT is a parameter to smooth the pressure forcing, for which we use $\Delta T = \pi/2\omega$.

Appendix B. Two-point correlations of turbulence velocity fluctuations

The two-point correlations of the turbulence fluctuation velocity are calculated to evaluate whether the domain size is sufficiently large to capture the coherent structures in the turbulent flow. The two-point auto-correlation for the velocity fluctuation u_i', $R_{u_i'}$, is defined as

$$R_{u_i'}(r, z) = \frac{\langle u_i'(\boldsymbol{x}) u_i'(\boldsymbol{x} + r\hat{\boldsymbol{e}}_1)\rangle_{xy}}{\langle u_i'(\boldsymbol{x}) u_i'(\boldsymbol{x})\rangle_{xy}}. \tag{B 1}$$

Here, $\hat{\boldsymbol{e}}_1$ is the unit vector in the x-direction, and $R_{u_i'}$ is defined based on the average on a horizontal x–y plane, $\langle\cdot\rangle_{xy}$. As shown in figure 25(*a*), for case L1, the correlation functions $R_{u_i'}$ of different velocity components fall off to almost zero at the mid-point of the domain (less than 0.05), which is usually considered to be small enough in different types of turbulent flows (Komminaho, Lundbladh & Johansson 1996; Zikanov, Slinn & Dhanak 2003). The studies of the effect of the domain size for plane Couette flows by Komminaho *et al.* (1996) and Tsukahara, Kawamura & Shingai (2006) also show that the flow statistics only vary slightly when the correlation function at the mid-point of the domain decreases from 0.2 to 0.05. Among the three components, the spanwise velocity fluctuations have a relatively strong correlation, corresponding to the elongated streamwise vortices (Teixeira & Belcher 2010). Figure 25(*b*) shows that the correlation functions for the spanwise velocity fluctuations, $R_{v'}$, are sufficiently small for all cases considered in this study, and thus the domain size is sufficiently large.

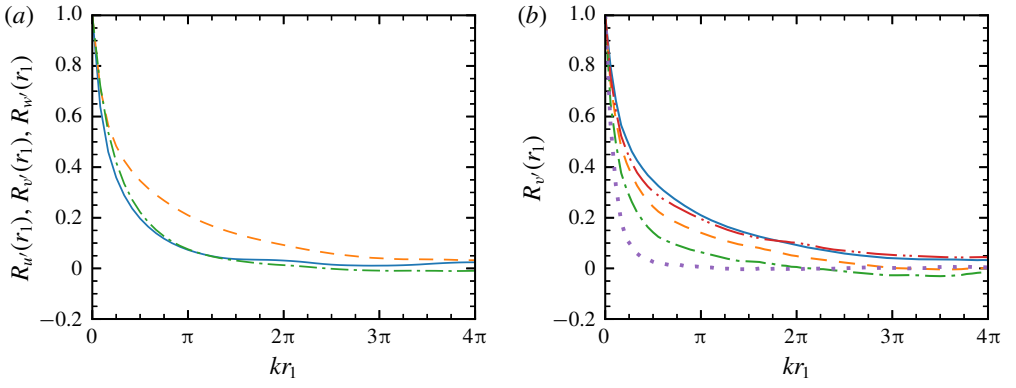

FIGURE 25. (Colour online) Two-point auto-correlation of velocity fluctuations. (*a*) $R_{u'_i}(kr_1)$ of the streamwise (——), spanwise (– – –) and vertical velocity (— · —) at $kz = -0.1$ for case L1; (*b*) $R_{v'}$ at $kz = -0.1$ for cases L1 (——), L1S (— · · —), L2 (– – –), L3 (— · —) and the shear-driven turbulence case S (· · · · · ·). Only half of the domain size is plotted due to the periodicity.

Appendix C. Linear stochastic estimation of coherent vortex structure

The linear stochastic estimation (LSE) is the linear least squares approximation of a random variable with respect to a conditioning event (Adrian & Moin 1988; Adrian 1994). Here, the conditioning event is chosen to be the presence of a vortex identified by the swirling strength λ_{ci} (Zhou *et al.* 1999; Christensen & Adrian 2001), the imaginary part of the complex eigenvalues of the velocity gradient tensor $\nabla \boldsymbol{u}$. The λ_{ci} is always non-negative, and it measures the strength of the rotation, but not the direction. To avoid the cancellation between the vortices of the opposite rotating directions when performing the LSE, we employ a signed swirling strength Λ_{ci} (Wu & Christensen 2006) as the conditioning event,

$$\Lambda_{ci} = \lambda_{ci} \frac{\omega_x}{|\omega_x|}. \tag{C 1}$$

Here, ω_x is used to decide the sign because of the dominance of the streamwise vortices. The LSE of a quantity f subject to the event Λ_{ci}, denoted by $\langle f(\boldsymbol{x}')|\Lambda_{ci}(\boldsymbol{x})\rangle$, is given by

$$\langle f(\boldsymbol{x}')|\Lambda_{ci}(\boldsymbol{x}) > 0\rangle = \frac{\langle \Lambda_{ci}(\boldsymbol{x}) f(\boldsymbol{x}+\boldsymbol{x}')\rangle_+}{\langle \Lambda_{ci}(\boldsymbol{x})\Lambda_{ci}(\boldsymbol{x})\rangle_+}\Lambda_{ci}(\boldsymbol{x}), \tag{C 2a}$$

$$\langle f(\boldsymbol{x}')|\Lambda_{ci}(\boldsymbol{x}) < 0\rangle = \frac{\langle \Lambda_{ci}(\boldsymbol{x}) f(\boldsymbol{x}+\boldsymbol{x}')\rangle_-}{\langle \Lambda_{ci}(\boldsymbol{x})\Lambda_{ci}(\boldsymbol{x})\rangle_-}\Lambda_{ci}(\boldsymbol{x}), \tag{C 2b}$$

where $\langle\cdot\rangle_+$ and $\langle\cdot\rangle_-$ denote that the averaging is taken at all locations of $\Lambda_{ci} > 0$ and $\Lambda_{ci} < 0$, respectively, and $\boldsymbol{x}'$ denotes the coordinates relative to $\boldsymbol{x}$. The above definition of LSE allows the vortices of opposite rotation directions to be averaged separately.

Appendix D. Calculation of correlation terms

Substituting (6.13) into the correlation term in (6.7*a*), we have

$$\overline{\omega_x^l\left(\frac{\partial u_w}{\partial x}\right)^l}^L \approx \overline{\left[\overline{\omega_x}^L\int\left(\frac{\partial u_w}{\partial x}\right)^l\mathrm{d}t+\overline{\omega_z}^L\int\left(\frac{\partial u_w}{\partial z}\right)^l\mathrm{d}t\right]\left(\frac{\partial u_w}{\partial x}\right)^l}^L$$
$$=\overline{\omega_x}^L\overline{\int\left(\frac{\partial u_w}{\partial x}\right)^l\mathrm{d}t\left(\frac{\partial u_w}{\partial x}\right)^l}^L+\overline{\omega_z}^L\overline{\int\left(\frac{\partial u_w}{\partial z}\right)^l\mathrm{d}t\left(\frac{\partial u_w}{\partial x}\right)^l}^L. \quad (D\,1)$$

If we use the linear wave expression,

$$\left(\frac{\partial u_w}{\partial x}\right)^l=-\left(\frac{\partial w_w}{\partial z}\right)^l\approx ak\omega\mathrm{e}^{kz}\cos\varphi, \quad (D\,2)$$
$$\left(\frac{\partial u_w}{\partial z}\right)^l=\left(\frac{\partial w_w}{\partial x}\right)^l\approx ak\omega\mathrm{e}^{kz}\sin\varphi, \quad (D\,3)$$

where $\varphi=kx-\omega t$ is the wave phase. We can see that in the first term of (D 1), the phase difference between $\int(\partial u_w/\partial x)^l\mathrm{d}t$ and $(\partial u_w/\partial x)^l$ is $\pi/2$. As a result, the Lagrangian average (2.16) of the product of these two variables has a negligible net effect. In the second term of (D 1), the values of $\int(\partial u_w/\partial z)^l\mathrm{d}t$ and $(\partial u_w/\partial x)^l$ are positively correlated and yield a net contribution as

$$\overline{\omega_x^l\left(\frac{\partial u_w}{\partial x}\right)^l}^L\approx\overline{\omega_z}^L\overline{\int\left(\frac{\partial u_w}{\partial z}\right)^l\mathrm{d}t\left(\frac{\partial u_w}{\partial x}\right)^l}^L\approx 0.5\,\overline{\omega_z}^L\mathrm{e}^{2kz}(ak)^2\omega. \quad (D\,4)$$

Similarly, we can calculate the correlation term in (6.7*b*) as

$$\overline{\omega_z^l\left(\frac{\partial u_w}{\partial z}\right)^l}^L \approx \overline{\left[\overline{\omega_x}^L\int\left(\frac{\partial w_w}{\partial x}\right)^l\mathrm{d}t+\overline{\omega_z}^L\int\left(\frac{\partial w_w}{\partial z}\right)^l\mathrm{d}t\right]\left(\frac{\partial u_w}{\partial z}\right)^l}^L$$
$$=\overline{\omega_x}^L\overline{\int\left(\frac{\partial w_w}{\partial x}\right)^l\mathrm{d}t\left(\frac{\partial u_w}{\partial z}\right)^l}^L+\overline{\omega_z}^L\overline{\int\left(\frac{\partial w_w}{\partial z}\right)^l\mathrm{d}t\left(\frac{\partial u_w}{\partial z}\right)^l}^L$$
$$=\overline{\omega_z}^L\overline{\int\left(\frac{\partial w_w}{\partial z}\right)^l\mathrm{d}t\left(\frac{\partial u_w}{\partial z}\right)^l}^L\approx 0.5\,\overline{\omega_z}^L\mathrm{e}^{2kz}(ak)^2\omega. \quad (D\,5)$$

Here, the first term has no contribution because the phase difference between $\int(\partial w_w/\partial x)^l\mathrm{d}t$ and $(\partial u_w/\partial z)^l$ is $\pi/2$.

Using (6.13) and (D 3), we can calculate the correlation terms in (6.7*c*) and (6.7*d*) as

$$\overline{\omega_x^l\left(\frac{\partial w_w}{\partial x}\right)^l}^L \approx \overline{\left[\overline{\omega_x}^L\int\left(\frac{\partial u_w}{\partial x}\right)^l\mathrm{d}t+\overline{\omega_z}^L\int\left(\frac{\partial u_w}{\partial z}\right)^l\mathrm{d}t\right]\left(\frac{\partial w_w}{\partial x}\right)^l}^L$$
$$=\overline{\omega_x}^L\overline{\int\left(\frac{\partial u_w}{\partial x}\right)^l\mathrm{d}t\left(\frac{\partial w_w}{\partial x}\right)^l}^L+\overline{\omega_z}^L\overline{\int\left(\frac{\partial u_w}{\partial z}\right)^l\mathrm{d}t\left(\frac{\partial w_w}{\partial x}\right)^l}^L$$
$$\approx\overline{\omega_x}^L\overline{\int\left(\frac{\partial u_w}{\partial x}\right)^l\mathrm{d}t\left(\frac{\partial w_w}{\partial x}\right)^l}^L\approx -0.5\,\overline{\omega_x}^L\mathrm{e}^{2kz}akS, \quad (D\,6)$$

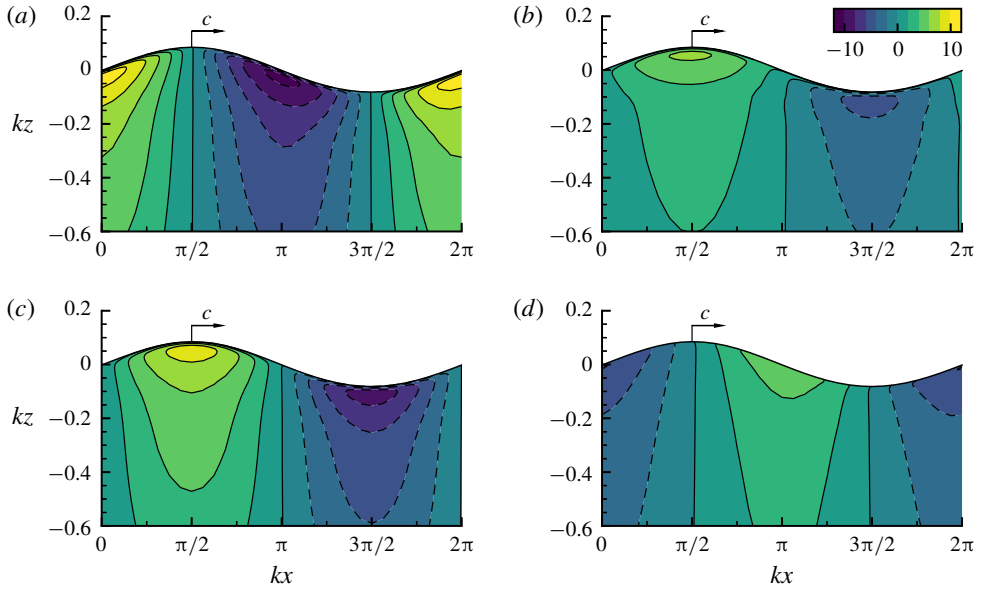

FIGURE 26. (Colour online) Contours of the terms of the wave distortion $\mathcal{D}^w$ in the flow with $Re_\tau = 500$: (*a*) $\langle \omega_x \partial u_w/\partial x \rangle$, (*b*) $\langle \omega_z \partial u_w/\partial z \rangle$, (*c*) $\langle \omega_x \partial w_w/\partial x \rangle$ and (*d*) $\langle \omega_z \partial w_w/\partial z \rangle$.

$$\begin{aligned}\overline{\omega_z^l\left(\frac{\partial w_w}{\partial z}\right)^l}^L &\approx \overline{\left[\overline{\omega_x}^L\int\left(\frac{\partial w_w}{\partial x}\right)^l \mathrm{d}t + \overline{\omega_z}^L\int\left(\frac{\partial w_w}{\partial z}\right)^l \mathrm{d}t\right]\left(\frac{\partial w_w}{\partial z}\right)^l}^L \\ &= \overline{\omega_x}^L\overline{\int\left(\frac{\partial w_w}{\partial x}\right)^l \mathrm{d}t\left(\frac{\partial w_w}{\partial z}\right)^l}^L + \overline{\omega_z}^L\overline{\int\left(\frac{\partial w_w}{\partial z}\right)^l \mathrm{d}t\left(\frac{\partial w_w}{\partial z}\right)^l}^L \\ &\approx \overline{\omega_x}^L\overline{\int\left(\frac{\partial w_w}{\partial x}\right)^l \mathrm{d}t\left(\frac{\partial w_w}{\partial z}\right)^l}^L \approx -0.5\,\overline{\omega_x}^L \mathrm{e}^{2kz}akS. \end{aligned} \tag{D 7}$$

In (D 6), the phase difference between $\int (\partial u_w/\partial z)^l \mathrm{d}t$ and $(\partial w_w/\partial x)^l$ is $\pi/2$ and the corresponding term is omitted. The same applies to $\overline{\int (\partial w_w/\partial z)^l \mathrm{d}t (\partial w_w/\partial z)^l}^L$ in (D 7).

Appendix E. Reynolds number effect

To investigate whether the dominant mechanism of the wave effect on the vorticity evolution is affected by the Reynolds number, a simulation of Langmuir turbulence with $Re_\tau = 500$ is carried out. The remaining parameters are the same as those of case L1 (table 1). The grid size is $128 \times 160 \times 73$ and the resolution satisfies the criteria for wall-resolved LES.

Figure 26 shows the wave distortion terms $\mathcal{D}^w$ as in figure 17. The positive and negative regions and the vertical distribution of the terms are similar to those in the flow at $Re_\tau = 2000$. This indicates that the vorticity fluctuations due to the stretching and tilting by the wave orbital straining are similar at the two different Reynolds numbers.

Figures 27(*a*) and 27(*b*) show the Lagrangian decomposition of the wave distortion effect for the evolution of $\overline{\omega_x}^L$ and $\overline{\omega_z}^L$ (6.7), respectively. Compared with figures 21(*a*)

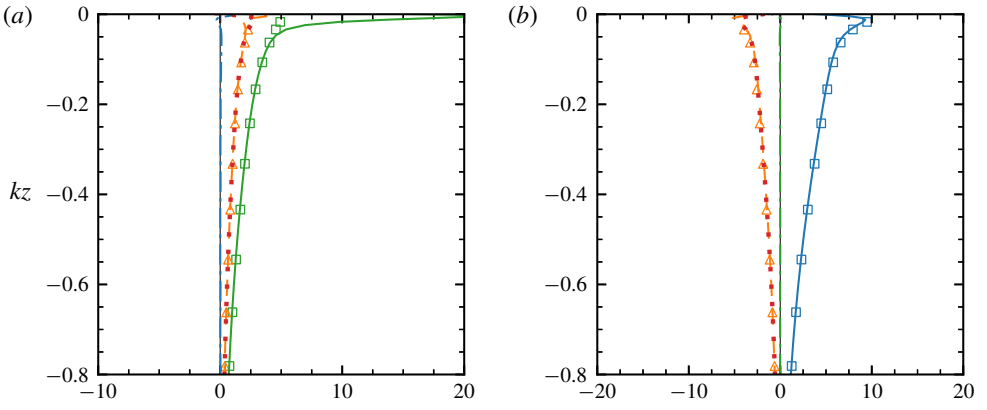

FIGURE 27. (Colour online) Lagrangian decomposition of the wave distortion term (*a*) $\overline{\mathcal{D}_x^w}^L$ ((6.7*a*) and (6.7*b*)) and (*b*) $\overline{\mathcal{D}_z^w}^L$ ((6.7*c*) and (6.7*d*)) in the flow with $Re_\tau = 500$. See the captions of figures 21 and 22 for the meanings of the line types in (*a*) and (*b*), respectively.

and 22(*a*), these profiles are very similar. For the dynamics of $\overline{\omega_x}^L$, both the mean effect and the phase correlation between the vorticity fluctuations and the wave orbital straining result in a net enhancement of the streamwise vorticity. Meanwhile for the evolution of $\overline{\omega_z}^L$, the mean effect is cancelled by the correlation effect. In addition, the theoretical predictions, (6.9), (6.11), (6.14) and (6.15), agree with the numerical results. The above comparisons show that although the Reynolds number can affect the flow statistics quantitatively, the mechanisms of the vorticity dynamics under the distortion of the surface wave appear to be the same.

REFERENCES

ADRIAN, R. J. 1994 Stochastic estimation of conditional structure: a review. *Appl. Sci. Res.* **53** (3-4), 291–303.

ADRIAN, R. J. & MOIN, P. 1988 Stochastic estimation of organized turbulent structure: Homogeneous shear flow. *J. Fluid Mech.* **190**, 531–559.

ANDREWS, D. G. & MCINTYRE, M. E. 1978 An exact theory of nonlinear waves on a Lagrangian-mean flow. *J. Fluid Mech.* **89** (04), 609–646.

ARDHUIN, F. & JENKINS, A. D. 2006 On the interaction of surface waves and upper ocean turbulence. *J. Phys. Oceanogr.* **36** (3), 551–557.

ARDHUIN, F., RASCLE, N. & BELIBASSAKIS, K. 2008 Explicit wave-averaged primitive equations using a generalized Lagrangian mean. *Ocean Model.* **20** (1), 35–60.

BELCHER, S. E., GRANT, A. L. M., HANLEY, K. E., FOX-KEMPER, B., VAN ROEKEL, L., SULLIVAN, P. P., LARGE, W. G., BROWN, A., HINES, A., CALVERT, D. *et al.* 2012 A global perspective on Langmuir turbulence in the ocean surface boundary layer. *Geophys. Res. Lett.* **39** (18), L18605.

BHASKARAN, R. & LEIBOVICH, S. 2002 Eulerian and Lagrangian Langmuir circulation patterns. *Phys. Fluids* **14** (7), 2557–2571.

BOU-ZEID, E., MENEVEAU, C. & PARLANGE, M. 2005 A scale-dependent Lagrangian dynamic model for large eddy simulation of complex turbulent flows. *Phys. Fluids* **17** (2), 025105.

CHAPMAN, D. R. 1979 Computational aerodynamics development and outlook. *AIAA J.* **17** (12), 1293–1313.

CHEN, B., YANG, D., MENEVEAU, C. & CHAMECKI, M. 2016 Effects of swell on transport and dispersion of oil plumes within the ocean mixed layer. *J. Geophys. Res.-Oceans* **121** (5), 3564–3578.

CHOI, H. & MOIN, P. 2012 Grid-point requirements for large eddy simulation: Chapman's estimates revisited. *Phys. Fluids* **24** (1), 011702.

CHRISTENSEN, K. T. & ADRIAN, R. J. 2001 Statistical evidence of hairpin vortex packets in wall turbulence. *J. Fluid Mech.* **431**, 433–443.

CRAIK, A. D. D. 1977 The generation of Langmuir circulations by an instability mechanism. *J. Fluid Mech.* **81** (02), 209–223.

CRAIK, A. D. D. 1982 Wave-induced longitudinal-vortex instability in shear flows. *J. Fluid Mech.* **125**, 37–52.

CRAIK, A. D. D. & LEIBOVICH, S. 1976 A rational model for Langmuir circulations. *J. Fluid Mech.* **73** (03), 401–426.

D'ASARO, E. A. 2014 Turbulence in the upper-ocean mixed layer. *Annu. Rev. Mar. Sci.* **6**, 101–115.

DENG, B.-Q., YANG, Z., XUAN, A. & SHEN, L. 2019 Influence of Langmuir circulations on turbulence in the bottom boundary layer of shallow water. *J. Fluid Mech.* **861**, 275–308.

DIMAS, A. A. & FIALKOWSKI, L. T. 2000 Large-wave simulation (LWS) of free-surface flows developing weak spilling breaking waves. *J. Comput. Phys.* **159** (2), 172–196.

FAN, Y. & GRIFFIES, S. M. 2014 Impacts of parameterized Langmuir turbulence and nonbreaking wave mixing in global climate simulations. *J. Clim.* **27** (12), 4752–4775.

FARMER, D. & LI, M. 1995 Patterns of bubble clouds organized by Langmuir circulation. *J. Phys. Oceanogr.* **25** (6), 1426–1440.

FENTON, J. D. 1985 A fifth-order Stokes theory for steady waves. *J. Waterways Port Coast. Ocean Div. ASCE* **111** (2), 216–234.

FUJIWARA, Y., YOSHIKAWA, Y. & MATSUMURA, Y. 2018 A Wave-resolving simulation of langmuir circulations with a nonhydrostatic free-surface model: comparison with Craik–Leibovich theory and an alternative Eulerian view of the driving mechanism. *J. Phys. Oceanogr.* **48** (8), 1691–1708.

GANAPATHISUBRAMANI, B., LONGMIRE, E. K. & MARUSIC, I. 2003 Characteristics of vortex packets in turbulent boundary layers. *J. Fluid Mech.* **478**, 35–46.

GERMANO, M., PIOMELLI, U., MOIN, P. & CABOT, W. H. 1991 A dynamic subgrid-scale eddy viscosity model. *Phys. Fluids* **3** (7), 1760–1765.

GNANADESIKAN, A. & WELLER, R. A. 1995 Structure and instability of the Ekman spiral in the presence of surface gravity waves. *J. Phys. Oceanogr.* **25** (12), 3148–3171.

GRANT, A. L. M. & BELCHER, S. E. 2009 Characteristics of Langmuir turbulence in the ocean mixed layer. *J. Phys. Oceanogr.* **39** (8), 1871–1887.

GUO, X. & SHEN, L. 2009 On the generation and maintenance of waves and turbulence in simulations of free-surface turbulence. *Comput. Phys.* **228** (19), 7313–7332.

GUO, X. & SHEN, L. 2013 Numerical study of the effect of surface waves on turbulence underneath. Part 1. Mean flow and turbulence vorticity. *J. Fluid Mech.* **733**, 558–587.

GUO, X. & SHEN, L. 2014 Numerical study of the effect of surface wave on turbulence underneath. Part 2. Eulerian and Lagrangian properties of turbulence kinetic energy. *J. Fluid Mech.* **744**, 250–272.

GUTIÉRREZ, P. & AUMAÎTRE, S. 2016 Surface waves propagating on a turbulent flow. *Phys. Fluids* **28** (2), 025107.

HARCOURT, R. R. & D'ASARO, E. A. 2008 Large-eddy simulation of Langmuir turbulence in pure wind seas. *J. Phys. Oceanogr.* **38** (7), 1542–1562.

HODGES, B. R. & STREET, R. L. 1999 On simulation of turbulent nonlinear free-surface flows. *Comput. Phys.* **151** (2), 425–457.

JEONG, J. & HUSSAIN, F. 1995 On the identification of a vortex. *J. Fluid Mech.* **285**, 69–94.

JIANG, J.-Y. & STREET, R. L. 1991 Modulated flows beneath wind-ruffled, mechanically generated water waves. *J. Geophys. Res.-Oceans* **96** (C2), 2711–2721.

KAWAMURA, T. 2000 Numerical investigation of turbulence near a sheared air–water interface. Part 2. Interaction of turbulent shear flow with surface waves. *J. Mar. Sci. Technol.* **5** (4), 161–175.

KIDA, S. & TANAKA, M. 1994 Dynamics of vortical structures in a homogeneous shear flow. *J. Fluid Mech.* **274**, 43–68.

KIM, J. & MOIN, P. 1985 Application of a fractional-step method to incompressible Navier–Stokes equations. *J. Comput. Phys.* **59**, 308–323.

KIRBY, J. T. & CHEN, T.-M. 1989 Surface waves on vertically sheared flows: approximate dispersion relations. *J. Geophys. Res.-Oceans* **94** (C1), 1013–1027.

KLEWICKI, J. C., METZGER, M. M., KELNER, E. & THURLOW, E. M. 1995 Viscous sublayer flow visualizations at $R\theta \simeq 1\,500\,000$. *Phys. Fluids* **7** (4), 857–863.

KOMMINAHO, J., LUNDBLADH, A. & JOHANSSON, A. V. 1996 Very large structures in plane turbulent Couette flow. *J. Fluid Mech.* **320**, 259–285.

KUKULKA, T., PLUEDDEMANN, A. J., TROWBRIDGE, J. H. & SULLIVAN, P. P. 2009 Significance of Langmuir circulation in upper ocean mixing: comparison of observations and simulations. *Geophys. Res. Lett.* **36** (10), L10603.

LANGMUIR, I. 1938 Surface motion of water induced by wind. *Science* **87** (2250), 119–123.

LEIBOVICH, S. 1977*a* Convective instability of stably stratified water in the ocean. *J. Fluid Mech.* **82** (03), 561–581.

LEIBOVICH, S. 1977*b* On the evolution of the system of wind drift currents and Langmuir circulations in the ocean. Part 1. Theory and averaged current. *J. Fluid Mech.* **79** (04), 715–743.

LEIBOVICH, S. 1980 On wave-current interaction theories of Langmuir circulations. *J. Fluid Mech.* **99** (04), 715–724.

LEIBOVICH, S. 1983 The form and dynamics of Langmuir circulations. *Annu. Rev. Fluid Mech.* **15**, 391–427.

LEIBOVICH, S. & PAOLUCCI, S. 1980 Energy stability of the Eulerian-mean motion in the upper ocean to three-dimensional perturbations. *Phys. Fluids* **23** (7), 1286–1290.

LEIBOVICH, S. & PAOLUCCI, S. 1981 The instability of the ocean to Langmuir circulations. *J. Fluid Mech.* **102**, 141–167.

LEWIS, D. M. 2005 A simple model of plankton population dynamics coupled with a LES of the surface mixed layer. *J. Theor. Biol.* **234** (4), 565–591.

LI, M. 2000 Estimating horizontal dispersion of floating particles in wind-driven upper ocean. *Spill Sci. Technol. B.* **6** (3–4), 255–261.

LI, M. & GARRETT, C. 1993 Cell merging and the jet/downwelling ratio in Langmuir circulation. *J. Mar. Res.* **51** (4), 737–769.

LI, M., GARRETT, C. & SKYLLINGSTAD, E. 2005 A regime diagram for classifying turbulent large eddies in the upper ocean. *Deep-Sea Res.* I **52** (2), 259–278.

LI, Q., WEBB, A., FOX-KEMPER, B., CRAIG, A., DANABASOGLU, G., LARGE, W. G. & VERTENSTEIN, M. 2016 Langmuir mixing effects on global climate: WAVEWATCH III in CESM. *Ocean Model.* **103**, 145–160.

LONGUET-HIGGINS, M. S. 1953 Mass transport in water waves. *Phil. Trans. R. Soc. Lond. A* **245** (903), 535–581.

LONGUET-HIGGINS, M. S. 1986 Eulerian and Lagrangian aspects of surface waves. *J. Fluid Mech.* **173**, 683–707.

MAGNAUDET, J. & THAIS, L. 1995 Orbital rotational motion and turbulence below laboratory wind water waves. *J. Geophys. Res.-Oceans* **100** (C1), 757–771.

MCWILLIAMS, J. C., HUCKLE, E., LIANG, J. & SULLIVAN, P. P. 2013 Langmuir turbulence in swell. *J. Phys. Oceanogr.* **44** (3), 870–890.

MCWILLIAMS, J. C. & SULLIVAN, P. P. 2000 Vertical mixing by Langmuir circulations. *Spill Sci. Technol. B.* **6** (3–4), 225–237.

MCWILLIAMS, J. C., SULLIVAN, P. P. & MOENG, C.-H. 1997 Langmuir turbulence in the ocean. *J. Fluid Mech.* **334**, 1–30.

MELVILLE, W. K., SHEAR, R. & VERON, F. 1998 Laboratory measurements of the generation and evolution of Langmuir circulations. *J. Fluid Mech.* **364**, 31–58.

MENEVEAU, C., LUND, T. S. & CABOT, W. H. 1996 A Lagrangian dynamic subgrid-scale model of turbulence. *J. Fluid Mech.* **319**, 353–385.

MOIN, P. & KIM, J. 1985 The structure of the vorticity field in turbulent channel flow. Part 1. Analysis of instantaneous fields and statistical correlations. *J. Fluid Mech.* **155**, 441–464.

MORRIS, S. C., STOLPA, S. R., SLABOCH, P. E. & KLEWICKI, J. C. 2007 Near-surface particle image velocimetry measurements in a transitionally rough-wall atmospheric boundary layer. *J. Fluid Mech.* **580**, 319–338.

PHILLIPS, O. M. 1977 *The Dynamics of the Upper Ocean*, 2nd edn. Cambridge University Press.

PHILLIPS, W. R. C. 2002 Langmuir circulations beneath growing or decaying surface waves. *J. Fluid Mech.* **469**, 317–342.

PHILLIPS, W. R. C. & WU, Z. 1994 On the instability of wave-catalysed longitudinal vortices in strong shear. *J. Fluid Mech.* **272**, 235–254.

PIOMELLI, U. & BALARAS, E. 2002 Wall-layer models for large-eddy simulations. *Annu. Rev. Fluid Mech.* **34** (1), 349–374.

POLONICHKO, V. 1997 Generation of Langmuir circulation for nonaligned wind stress and the Stokes drift. *J. Geophys. Res.-Oceans* **102** (C7), 15773–15780.

PORTÉ-AGEL, F., MENEVEAU, C. & PARLANGE, M. B. 2000 A scale-dependent dynamic model for large-eddy simulation: application to a neutral atmospheric boundary layer. *J. Fluid Mech.* **415**, 261–284.

RABE, T. J., KUKULKA, T., GINIS, I., HARA, T., REICHL, B. G., D'ASARO, E. A., HARCOURT, R. R. & SULLIVAN, P. P. 2014 Langmuir turbulence under Hurricane Gustav (2008). *J. Phys. Oceanogr.* **45** (3), 657–677.

RASHIDI, M., HETSRONI, G. & BANERJEE, S. 1992 Wave–turbulence interaction in free-surface channel flows. *Phys. Fluids* A **4** (12), 2727–2738.

SHEN, L., ZHANG, X., YUE, D. K. P. & TRIANTAFYLLOU, G. S. 1999 The surface layer for free-surface turbulent flows. *J. Fluid Mech.* **386**, 167–212.

SKYLLINGSTAD, E. D. & DENBO, D. W. 1995 An ocean large-eddy simulation of Langmuir circulations and convection in the surface mixed layer. *J. Geophys. Res.-Oceans* **100** (C5), 8501–8522.

STOKES, G. 1847 On the theory of oscillatory waves. *Trans. Camb. Phil. Soc.* **8**, 441–455.

STOLL, R. & PORTÉ-AGEL, F. 2006 Dynamic subgrid-scale models for momentum and scalar fluxes in large-eddy simulations of neutrally stratified atmospheric boundary layers over heterogeneous terrain. *Water Resour. Res.* **42** (1), W01409.

SULLIVAN, P. P. & MCWILLIAMS, J. C. 2010 Dynamics of winds and currents coupled to surface waves. *Annu. Rev. Fluid Mech.* **42**, 19–42.

SULLIVAN, P. P., ROMERO, L., MCWILLIAMS, J. C. & MELVILLE, W. K. 2012 Transient evolution of Langmuir turbulence in ocean boundary layers driven by hurricane winds and waves. *J. Phys. Oceanogr.* **42** (11), 1959–1980.

SWAN, C., CUMMINS, I. P. & JAMES, R. L. 2001 An experimental study of two-dimensional surface water waves propagating on depth-varying currents. Part 1. Regular waves. *J. Fluid Mech.* **428**, 273–304.

TEIXEIRA, M. A. C. & BELCHER, S. E. 2002 On the distortion of turbulence by a progressive surface wave. *J. Fluid Mech.* **458**, 229–267.

TEIXEIRA, M. A. C. & BELCHER, S. E. 2010 On the structure of Langmuir turbulence. *Ocean Model.* **31** (3–4), 105–119.

TEJADA-MARTÍNEZ, A. E. & GROSCH, C. E. 2007 Langmuir turbulence in shallow water. Part 2. Large-eddy simulation. *J. Fluid Mech.* **576**, 63–108.

TEJADA-MARTÍNEZ, A. E., GROSCH, C. E., GARGETT, A. E., POLTON, J. A., SMITH, J. A. & MACKINNON, J. A. 2009 A hybrid spectral/finite-difference large-eddy simulator of turbulent processes in the upper ocean. *Ocean Model.* **30** (2–3), 115–142.

THORPE, S. A. 2004 Langmuir circulation. *Annu. Rev. Fluid Mech.* **36**, 55–79.

THORPE, S. A., OSBORN, T. R., FARMER, D. M. & VAGLE, S. 2003 Bubble clouds and Langmuir circulation: observations and models. *J. Phys. Oceanogr.* **33** (9), 2013–2031.

TSAI, W.-T., CHEN, S.-M. & MOENG, C.-H. 2005 A numerical study on the evolution and structure of a stress-driven free-surface turbulent shear flow. *J. Fluid Mech.* **545**, 163–192.

TSUKAHARA, T., KAWAMURA, H. & SHINGAI, K. 2006 DNS of turbulent Couette flow with emphasis on the large-scale structure in the core region. *J. Turbul.* **7**, N19.

VAN ROEKEL, L. P., FOX-KEMPER, B., SULLIVAN, P. P., HAMLINGTON, P. E. & HANEY, S. R. 2012 The form and orientation of Langmuir cells for misaligned winds and waves. *J. Geophys. Res.-Oceans* **117** (C5), C05001.

VERON, F. & MELVILLE, W. K. 2001 Experiments on the stability and transition of wind-driven water surfaces. *J. Fluid Mech.* **446**, 25–65.

VERON, F., MELVILLE, W. K. & LENAIN, L. 2009 Measurements of ocean surface turbulence and wave–turbulence interactions. *J. Phys. Oceanogr.* **39** (9), 2310–2323.

VIVANCO, F. & MELO, F. 2004 Experimental study of surface waves scattering by a single vortex and a vortex dipole. *Phys. Rev.* E **69** (2), 026307.

WANG, P. & ÖZGÖKMEN, T. M. 2018 Langmuir circulation with explicit surface waves from moving-mesh modeling. *Geophys. Res. Lett.* **45** (1), 216–226.

WU, Y. & CHRISTENSEN, K. T. 2006 Population trends of spanwise vortices in wall turbulence. *J. Fluid Mech.* **568**, 55–76.

XUAN, A. & SHEN, L. 2019 A conservative scheme for simulation of free-surface turbulent and wave flows. *Comput. Phys.* **378**, 18–43.

YANG, D., CHAMECKI, M. & MENEVEAU, C. 2014*a* Inhibition of oil plume dilution in Langmuir ocean circulation. *Geophys. Res. Lett.* **41** (5), 1632–1638.

YANG, D., CHEN, B., CHAMECKI, M. & MENEVEAU, C. 2015 Oil plumes and dispersion in Langmuir, upper-ocean turbulence: large-eddy simulations and K-profile parameterization. *J. Geophys. Res.-Oceans* **120** (7), 4729–4759.

YANG, D., MENEVEAU, C. & SHEN, L. 2013 Dynamic modelling of sea-surface roughness for large-eddy simulation of wind over ocean wavefield. *J. Fluid Mech.* **726**, 62–99.

YANG, D., MENEVEAU, C. & SHEN, L. 2014*b* Effect of downwind swells on offshore wind energy harvesting – A large-eddy simulation study. *Renew. Energ.* **70**, 11–23.

YANG, D., MENEVEAU, C. & SHEN, L. 2014*c* Large-eddy simulation of offshore wind farm. *Phys. Fluids* **26** (2), 025101.

YANG, D. & SHEN, L. 2010 Direct-simulation-based study of turbulent flow over various waving boundaries. *J. Fluid Mech.* **650**, 131–180.

YANG, D. & SHEN, L. 2011 Simulation of viscous flows with undulatory boundaries. Part I. Basic solver. *Comput. Phys.* **230** (14), 5488–5509.

ZHANG, Z., CHINI, G. P., JULIEN, K. & KNOBLOCH, E. 2015 Dynamic patterns in the reduced Craik–Leibovich equations. *Phys. Fluids* **27** (4), 046605.

ZHOU, H. 1999 Numerical simulation of Langmuir circulations in a wavy domain and its comparison with the Craik–Leibovich theory. PhD thesis, Stanford University.

ZHOU, J., ADRIAN, R. J., BALACHANDAR, S. & KENDALL, T. M. 1999 Mechanisms for generating coherent packets of hairpin vortices in channel flow. *J. Fluid Mech.* **387**, 353–396.

ZIKANOV, O., SLINN, D. N. & DHANAK, M. R. 2003 Large-eddy simulations of the wind-induced turbulent Ekman layer. *J. Fluid Mech.* **495**, 343–368.